Water Modelling Studies to Predict Steel Quality in a 4 Strand Delta-Shaped Tundish

by

Shamik Kumar Ray

Department of Mining, Metals and Materials Engineering

McGill University

Montreal, Canada

February, 2006

A thesis submitted to the Faculty of Graduate Studies and Research in partial fulfillment of the requirements for the degree of

Masters of Engineering

Your file Votre référence
ISBN: 978-0-494-25011-2
Our file Notre référence
ISBN: 978-0-494-25011-2

ABSTRACT

Physical and mathematical modelling of fluid flow phenomena play an important role in studies of steel quality associated with the various steps in steelmaking and steel processing operations.

In the continuous casting process, the tundish not only serves as an intermediate buffer, but with increasing demands for high quality steel, it has also evolved into a useful reactor for liquid steel refining. It is now a proven fact that a modern tundish is designed to carry out different metallurgical operations such as inclusion separation and floatation, alloy trimming, superheat control, calcium doped inclusion modification, thermal and particulate homogenization.

To carry out those operations effectively, certain parameters like Residence Time Distribution (RTD), Residual Ratio of Inclusions (RRI), Slag Entrainment and Vortex formation phenomena are generally studied and optimized using various tundish designs, and flow modification devices. These are usually specific to a given plant practice and to a targeted grade of steel.

A full scale physical model of a delta shaped, four strand tundish using water as the simulating fluid for liquid steel was used to study the fluid flow behavior of a 12 t tundish producing aluminium-killed steel billets., The above mentioned parameters were studied to predict the performance of the tundish using two different types of flow modification systems.

RÉSUMÉ

Les modèles physique et mathématique des phénomènes d'écoulement de fluide, jouent un rôle important dans les études de la qualité d'acier, liées aux diverses étapes dans la fabrication et les procédures opérationnelles d'acier.

Dans le processus de coulée continue, le récipient de distribution sert non seulement d'amortisseur intermédiaire, mais avec l'augmentation des demandes d'acier de haute qualité, il s'est également transformé en un réacteur utile pour le raffinage en acier liquide. C'est maintenant un fait prouvé qu'un récipient de distribution moderne est conçu pour effectuer différentes opérations métallurgiques, telles que la séparation et la flottaison d'inclusion, réglage d'alliage, contrôle de surchauffage, modification d'inclusion enduite par calcium, l'homogénéisation thermique et des particules.

Pour effectuer ces opérations efficacement, certains paramètres comme les, 'residence time distribution' (RTD), rapport résiduel des inclusions (RRI), entraînement de scories et des phénomènes de formation de vortex, sont généralement étudiés et optimisés en utilisant de diverses conceptions de récipient de distribution, et modificateurs d'écoulement des fluides. Ce paramètres sont habituellement spécifiques à une pratique dans une usine et à une catégorie visée d'acier. Un modèle physique complet en forme delta, récipient de distribution avec quatre tuyaux d'écoulement, employant l'eau comme fluide de simulation pour l'acier liquide, a été employé pour étudier le comportement d'écoulement de fluide d'un récipient de distribution, de 12 tonnes produisant les billettes en acier calmé avec aluminium, les paramètres mentionnés ci-dessus, ont été étudiés pour prévoir la performance du récipient de distribution en utilisant deux types différents de systèmes de modification d'écoulement.

ACKNOWLEDGEMENTS

It is with deep sense of gratitude and sincere appreciation that I thank Prof. R.I.L. Guthrie for his constant encouragement and guidance, both intellectually and financially, during my masters program at McGill University. Similarly special thanks go to Dr. M. Isac for her constant help managing from carrying out experiments to the writing of reports.

I also thank Mr. R. Thibau and Mr. Alexandre Beaulieu of QIT without whom the modeling experiments would not have been possible. I am also grateful to the technicians, Mr. Alain Gagnon, Mr.Walter Greenland in the machine shop, for their help. Thanks also go to Mr Robert Paquette for his help during experiments.

I also thank my colleagues and friends, including Reza Afshar, Dan Humeniuc, Donghui Li, Hashem Mousavi and N. Tripathi for their help and constant encouragement during my experiments and study in this period. Special thanks goes to Dr. H.B. Kim, formerly of the MMPC, for his guidance during the initial periods of my experiments.

I would also like to thank Luis Calzado for giving his time and effort in translating my abstract into French.

Finally I would like to thank my supportive family, especially my wife Jayati, son Shiladitya, my father Sunil Roy, my mother Swagata Roy, my uncle Prof. Subhash C Ray and my aunt, the Late Shipra Ray, for their constant encouragement and support, without whom, I might not be able to complete the program.

NOMENCLATURE

A	: Projected area
A_p, A_{dp}	: Surface area plug volume, dispersed plug volume
$C_i(t)$	: Dimensionless concentration in ith strand at time t
C_i	: Instantaneous dimensionless concentration
C_{peak}	: Dimensionless peak concentration
d_p	: Diameter of particle
d_{noz}	: Diameter of nozzle
$E(t)$	: Residence time distribution function
$E_i(t)$	: Residence time distribution function for ith strand
f	: Drag coefficient
Gr	: Grashof number
g	: Acceleration due to gravity
g_i	: Component of acceleration due to gravity
H_{model}	: Depth of liquid in model
$H_{prototype}$	: Depth of liquid in prototype
H_{cr}	: Height of fluid when stable vortex is formed
h	: Depth of fluid
I	: Imposed current
K	: Strength of vortex
k	: Kinetic energy per unit volume
L	: Characteristic length
L_{model}	: Characteristic length in model
$L_{prototype}$	: Characteristic length in prototype
M	: Total mass
Δm_i	:Mass flowing out of ith strand at Δt

N_{Re} : Reynolds number

N_{Fr}, Fr : Froude number

N_{Eu} : Euler number

N_p :Rate of particle coalescence

N_{in} : Number of inclusions entering

N_{out} : Number of inclusions leaving

n_i : Number density of particle

p : Pressure

p^* : Dimensionless pressure

p_{ref} : Reference pressure

Q_{model} : Volumetric flow rate in model

$Q_{prototype}$: Volumetric flow rate in prototype

Q_a : Volumetric flow rate through active region

Q_d : Volumetric flow rate through dead region

Re_t : Turbulent Reynolds number

$\overline{R}$: Sum of radii of two coalescing particles

r : Radius

Tu : Thermal buoyancy number

Tu_{model} : Thermal buoyancy number for model

$Tu_{prototype}$: Thermal buoyancy number for prototype

T^* : Dimensionless temperature

T_0 : Initial temperature

T_{inlet} : Inlet temperature

ΔT_0 :Temperature change from reference

ΔT : Temperature change

$\Delta T_{\mathrm{model}}$: Temperature change in model

$\Delta T_{prototype}$: Temperature change in prototype

t : Time

t^* : Dimensionless time

$\bar{t}$: Nominal residence time

$t_{\min}$: Minimum break through time

t_{peak} : Time to attain peak concentration

t_{av} : Average residence time

U : Characteristic velocity

U_{model} : Characteristic velocity of model

$U_{prototype}$: Characteristic velocity of prototype

U_{in} : Inlet velocity

U_t, v_∞ : Terminal rising velocity

u_i, u_j : Velocity components

u^* : Dimensionless velocity

u : Velocity

u_i^*, u_j^* : Dimensionless velocity components

V : Volume

V_{pv}, V_p : Plug flow volume

V_{mv}, V_m : Mixed volume

V_{dv}, V_d : Dead volume

V_{dpv} : Dispersed plug flow volume

V_a : Active volume

ΔV : Voltage pulse

v : Volumetric flow rate

V_θ : Tangential velocity

V_r : Radial velocity

x_i, x_j :Distance component

x_i^*, x_j^* : Dimensionless distance component

λ : Scale factor

ρ : Density

ρ_l : Density of liquid

ρ_p : Density of particle

η, μ : Molecular viscosity

μ_{eff} : Effective viscosity

μ_{turb} : Turbulent viscosity

ρ_{water} : Density of water

ρ_{steel} : Density of steel

ρ^* : Dimensionless density

ρ_{ref} : Reference density

β : Coefficient of thermal expansion

β_{model} : Coefficient of thermal expansion for model

$\beta_{prototype}$: Coefficient of thermal expansion for prototype

ε : Rate of energy dissipation

υ : Kinematic viscosity

υ_l : Kinematic viscosity of liquid

$\overline{\theta}$: Dimensionless mean residence time

θ_c : Dimensionless mean residence time up to $\theta = 2$

θ_i : ith dimensionless time.

$\Delta\theta$: Change in dimensionless time

θ_{avg}, θ_{av} : Dimensionless average residence time

θ_{min} : Dimensionless minimum breakthrough time

θ_{peak} : Dimensionless time to attain peak concentration

ω : Angular velocity

∇^* : Dimensionless operator.

LIST OF FIGURES

Chapter 1

Figure 1.01 Schematic diagram of typical continuous casting process

Figure 1.02 Possible origins of oxide inclusions during continuous casting

Chapter 2

Figure 2.01 General nature of RTD curves (a) Ideal reactor, (b) Real reactor.

Figure 2.02 Schematic flow models and their associated theoretical flow curves (a) Mixed model, and (b) Modified mixed model

Figure 2.03 Flow through active and dead regions in combined model

Figure 2.04 A typical residence time distribution curve for flow in a tundish

Figure 2.05 Experimentally measured C curves in a water model of a single strand slab casting tundish system at various values of the dimensionless tundish width

Figure 2.06 Variation in drag coefficient with Reynolds number

Figure 2.07 Graphical representations of a line sink and line vortex

Figure 2.08 Streamlines for a vortex plus sink

Figure 2.09 General characteristics of funnel vortex

Figure 2.10 Different stages of vortex formation

Figure 2.11 Tangential velocities in the outer free vortex region at various depth and radii (A = nozzle radius)

Figure 2.12 Tangential velocities in the outer free vortex region at different horizontal levels

Figure 2.13 Radial velocities in the outer free vortex region at different depths and radii (A = nozzle radius)

Figure 2.14 Radial velocity distribution in horizontal plane at pipe-entrance level

Figure 2.15 Axial velocities near vortex core

Chapter 3

Figure 3.01 Full-scale plexi glass model of 4-strand delta shaped tundish.

Figure 3.02 Schematic views of the model tundish

Figure 3.03 RHI pad attached in the tundish

Figure 3.04 Diagram of the RHI pad

Figure 3.05 Optimized pad with 45^0 angled side lips attached in tundish

Figure 3.06 Cross section of side lip of the optimized pad

Figure 3.07 Schematic diagram of slag entrainment experimental setup

Figure 3.08 Experimental setup for vortex formation study

Figure 3.09 Experimental setup for inclusion separation

Figure 3.10 Principle of Electric Sensing Zone

Figure 3.11 Variation of voltage with concentration for channel 1

Figure 3.12 Variation of voltage with concentration for channel 2

Figure 3.13 Experimental setup for RTD experiment

Chapter 4

Figure 4.01 Schematic diagram of tundish to show the numbering of nozzles used in experiments

Figure 4.02 Comparative chart of collected number of beads of both inner and outer nozzles for both types of pads for 3 minutes drain time

Figure 4.03 Comparative chart of number of beads collected from the inner and outer nozzles for both types of pads following 5 minute drain times

Figure 4.04 Upper slag cover at steady state for new optimized pad

Figure 4.05 Upper slag layer at steady state with new optimized pad (pushing more beads near shroud)

Figure 4.06 Upper slag layer at steady state, using RHI pad

Figure 4.07 Critical liquid height for dimple formation (ie. at the start of vortex formation) over inner nozzles, 2&3

Figure 4.08 Critical liquid height for dimple formation (ie. at the start of vortex formation) over outer nozzles, 1&4

Figure 4.09 Average RRI% of inner and outer nozzles for RHI impact pad

Figure 4.10 Average RRI % of inner and outer nozzles with optimized pad
Figure 4.11 Comparative RRI % of inner and outer nozzles using optimized and RHI pad
Figure 4.12 Prediction of RRI% for RHI pad
Figure 4.13 Prediction of RRI% for optimized pad
Figure 4.14 Representative overall C curve using Optimized QIT pad
Figure 4.15 Representative C curve for Inner and outer nozzles using Optimized QIT pad
Figure 4.16 Representative overall C curve using RHI pad
Figure 4.17 Representative C curve for Inner and outer nozzles using RHI pad .

LIST OF TABLES

Table 3.01: Physical properties of water (20^0) and liquid steel (1600^0)

Table 4.01: Number of beads collected during a ladle change Vs nozzle numbers (5 min draining, with RHI pad)

Table 4.02: Number of beads collected during a ladle change Vs nozzle numbers (3 min draining, with RHI pad)

Table 4.03: Number of beads collected during a ladle change Vs nozzle numbers (3 min. draining, with Optimized Pad)

Table 4.04: Number of beads collected during a ladle change Vs nozzle numbers (5 min. draining, with Optimized Pad).

Table 4.05: Critical liquid height for dimple formation for RHI pad

Table 4.06: Critical liquid height for dimple formation for Optimized QIT pad

Table 4.07: Average number of particles & calculated RRI% Vs different size ranges for RHI pad

Table 4.08: Average number of particles & calculated RRI% Vs different size ranges for Optimized QIT pad

Table 4.09: Different variable calculated from C curve using Optimized QIT pad

Table 4.10: Different variable calculated from C curve using RHI pad

Table A.01: Physical properties of the materials used for modelling slag entrainment and those of liquid steel and slag.

Table A.02: Size of randomly sampled high-density polyethylene beads and their mean diameter

Table A.03: Mean bead size, Stoke's velocity and corresponding Reynolds numbers

Table A.04: Mean bead size, rise velocity and corresponding Reynolds numbers

Table A.05: Rise velocities, Diameter of the slag droplets, and Reynolds numbers

Table A.06: Physical properties of the materials used for modelling inclusion separation and those of liquid steel and dense alumina

Table A.07: Size of micro spheres & corresponding size of alumina inclusion considering behaviour in Stoke's region.

TABLE OF CONTENTS

ABSTRACT 2

RÉSUMÉ 3

ACKNOWLEDGEMENTS 4

NOMENCLATURE 5

LIST OF FIGURES 9

LIST OF TABLES 12

TABLE OF CONTENTS 14

1. INTRODUCTION

1.1 Introduction 16

1.2 Continuous casting 16

1.3 Motivation and context of present work 18

2. LITERATURE REVIEW

2.1 Similarity and modeling criteria study 20

2.2 Metallurgical performance study 26

2.2.1 Residence time distribution (RTD) 26

2.2.2 Direct measurement of inclusion seperation 38

2.3 Slag entrainment and vortex formation 41

3. EXPERIMENTAL PROCEDURE AND SETUP

3.1 Set up 52

3.2 Procedure

3.2.1 Slag entrainment 57

3.2.2 Vortex formation 58
3.2.3 Inclusion seperation 59
3.2.4 Residence time distribution 61
4. RESULTS AND DISCUSSION
4.1 Introduction 64
4.2 Slag entrainment 64
4.3 Vortex formation 74
4.4 Inclusion Separation Ratio 76
4.5 Residence time distribution 84
5. SUMMARY AND CONCLUSIONS 89
APPENDIX 1 90
APPENDIX 2 95
REFERENCES 97

1.INTRODUCTION

1.1 Introduction

In the continuous casting of steel, a tundish traditionally refers to an intermediate vessel placed between the ladle and the mould, designed to supply and distribute molten steel to different continuous casting moulds, at a near constant rate. With increasing demand of ultra high clean steel, tundishes are now acting as useful reactors where many metallurgical operations are carried out. Over its traditional role as a buffer, or steel distribution vessel, a modern day steelmaking tundish is designed to provide maximum opportunity for carrying out various metallurgical operations such as inclusion separation, flotation, alloy trimming of steel, calcium doped inclusion modification, superheat control, thermal and particulate homogenization[4].

1.2 Continuous casting

Though the continuous casting process for strip was conceived by Henry Bessemer in 1858, it only became widespread in the 1970s as a replacement to ingot casting. The continuous casting process has increased significantly since then and now, most of the steel makers follow this route. In 1992, continuous casting was used to produce over 90% of steel in the world, including carbon, alloy and stainless steel grades [45]. Wolf [45] quoted that the total world production of crude steel will increase to over 900 million tons per year in 2010 with steel produced by continuous casting still making up 90% of this production. But it is to be noted, the production of crude steel already had reached 1000 million tons per year mark.

Figure 1.01 shows a Schematic diagram of a typical continuous casting process for the production of slabs.

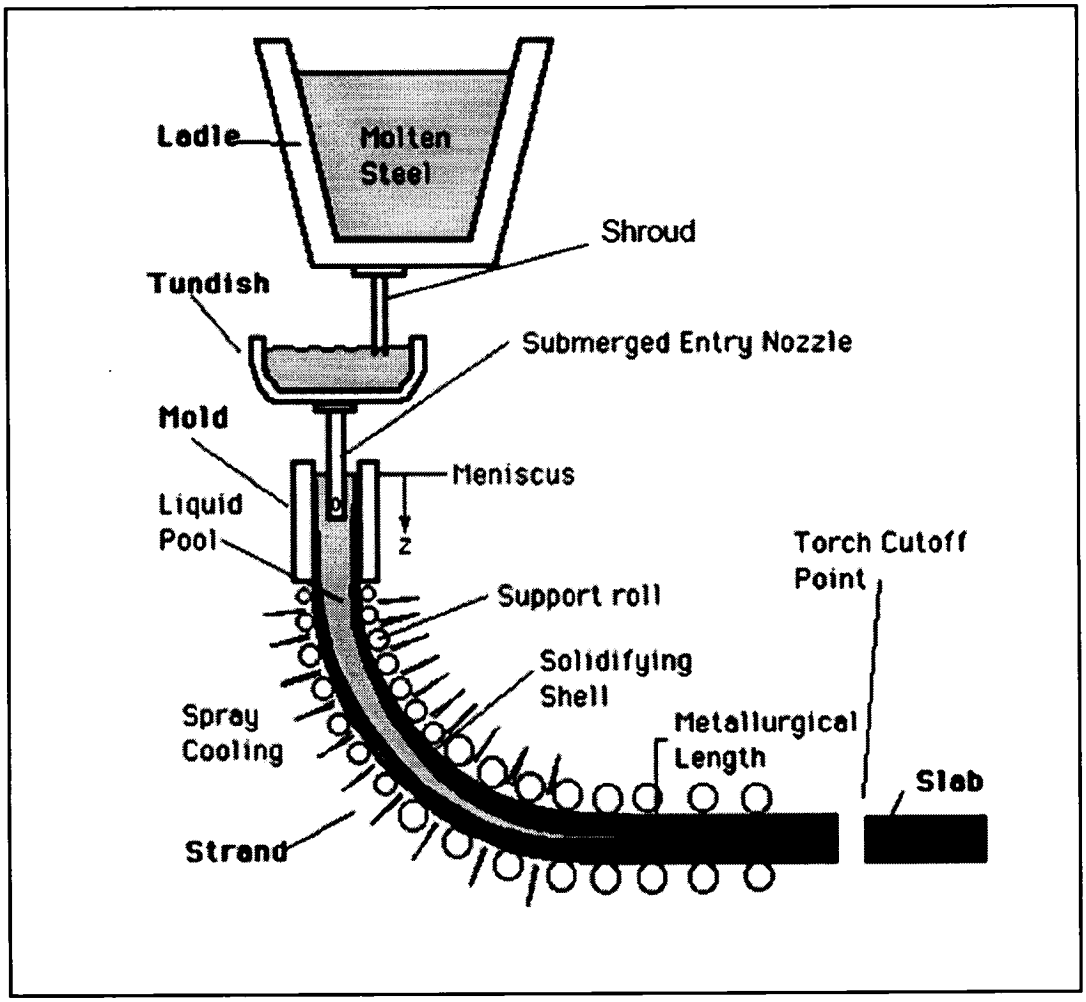

Figure 1.01: Schematic diagram of typical continuous casting process[10]

The relevant part of the continuous casting operation is described as below:

After secondary steelmaking operations, the ladle of steel is brought to the continuous caster where the steel is poured from the ladle through a shroud into the tundish. The shroud is used to shield the steel from the air when liquid steel flows from the ladle to the tundish. A control valve at the outlet of the ladle controls the flow rate into tundish. The liquid steel is again shielded from the air by a slag layer to prevent oxidation that would form detrimental oxide inclusions in the steel. The molten steel flows through the tundish and exits the tundish through the submerged entry nozzle (SEN) into a bottomless water cooled, oscillating copper mould, where it starts to solidify.

Between secondary steel making and casting in moulds, the steel gets contaminated with inclusions originating from different sources. Figure 1.02 shows the possible origin of

inclusions during the continuous casting process.

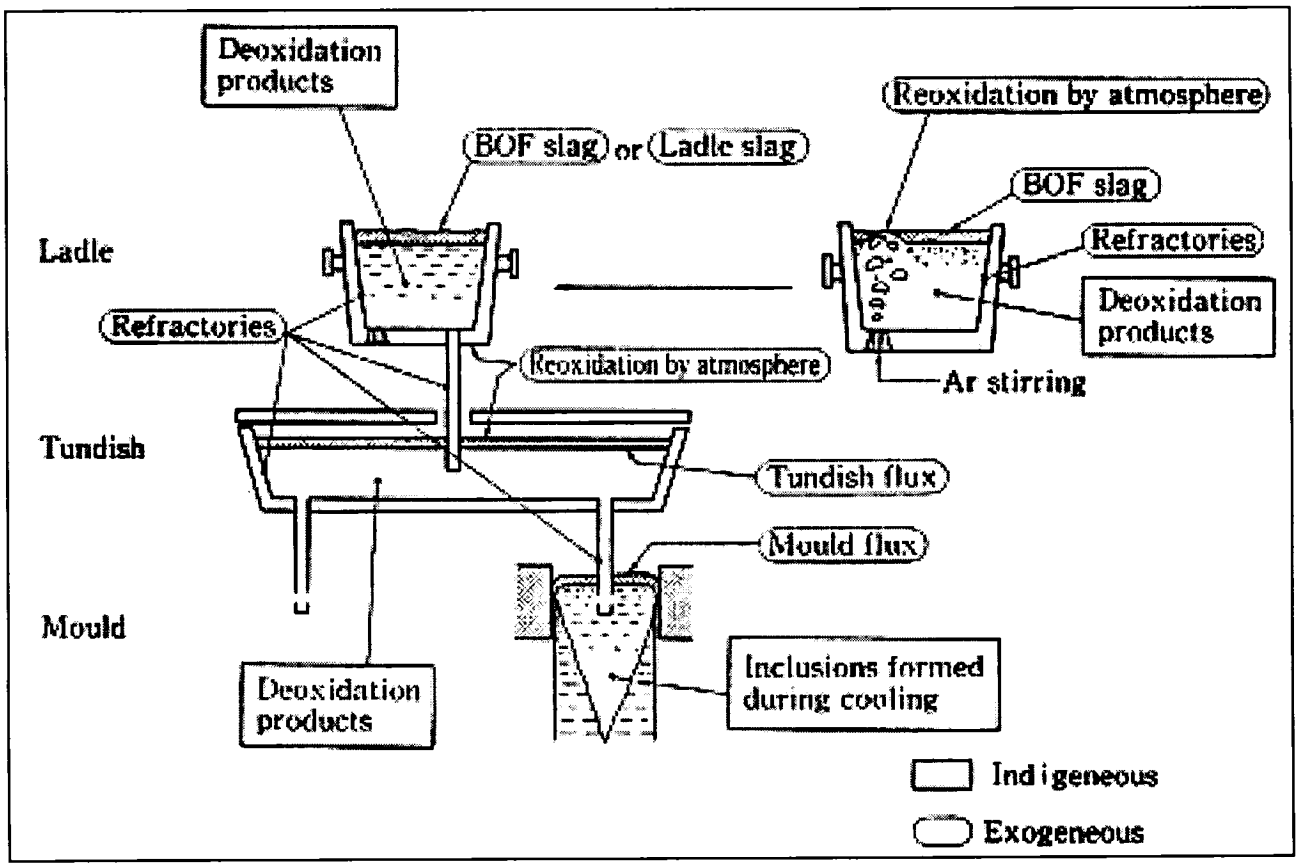

Figure 1.02: Possible origins of oxide inclusions during continuous casting [12]

1.3 Motivation and context of present work

Due to reoxidation, entrainment of slag etc., nonmetallic inclusions accumulate in liquid steel as it is transferred from ladle to mould via tundish. As can be seen that, before the start of solidification in the mould, the tundish is the last vessel where steel remains in the liquid state, all steel makers try to manipulate the liquid steel in the tundish so that they can feed cleaner steel to the mould. Being lighter than steel, the inclusions tend to float out to the upper slag layer. So sufficient time has to be given to complete the float out process. The more time an inclusion spends in tundish the higher is the probability for inclusion separation. So steel makers use different flow control devices to modify the

fluid flow pattern within the tundish to facilitate the floatation process and to avoid the entrainment of any slag within the tundish.

The main objective of this project is to study the performance of a delta shaped 4 strand tundish, which is used in QIT using different flow modifying device in terms of certain quantitatively measurable parameters, which are believed to represent the performance of the tundish. For this purpose, physical modeling was carried out using a full-scale plexi glass 4-strand delta shaped tundish and water as simulating liquid.

The quantifiable parameters used for the study are:

- Slag entrainment
- Vortexing height
- Residual ratio of inclusions
- Residence time distribution.

The results of this study can give the idea about the performance of the tundish with its flow modifiers and allow the steelmaker to take decisions prior to flow modifying devices in the real tundish.

2.LITERATURE REVIEW

According to Szekely et al.[21] the main objective of physical modeling is to achieve a realistic representation of a system using materials and equipment, with which measurements may be made conveniently and in a cost effective manner.

Water modeling in full or reduced scale model of a tundish is a very popular means of physical simulation of melt flow in tundishes. It is a relatively quick and inexpensive method for qualitative or quantitative studies of melt flows.

Physical modeling studies of tundish operations, reported in the literature, can be broadly divided in main two categories.

- Similarity and modelling criteria studies.
- Metallurgical performance studies.

In addition some researchers have also studied slag entrainment and vortexing hydrodynamics in order to understand the cause of one of the most important phenomena of entrapment of supernatant fluid during drainage from vessel.

2.1 Similarity and modelling criteria study

The actual criteria for realistic representation as mentioned earlier are more properly stated as **similarity criteria.**

If the same form of dimensionless velocity, temperature, pressure, or concentration field exists between the model and the prototype one can faithfully represent other. That means to fulfill the similarity criteria; there exist a constant ratio between corresponding quantities of prototype and the model [2].

The similarity criteria are divided in following categories:

- Geometrical similarity
- Mechanical similarity
- Thermal similarity
- Chemical similarity.

Geometrical similarity means for every point in prototype, there exists a corresponding point in the model. For obtaining geometrical similarity, a term **'scale factor'** λ, is kept constant for all dimensions.

$$\text{Where } \lambda = \frac{Length_{model}}{Length_{prototype}}$$

Mechanical similarity is subdivided in three categories, namely **static similarity, kinematic similarity, and dynamic similarity.**

Static similarity is concerned with solid bodies and structures. This is used to relate static loads, torques etc.

Kinematic similarity represents similarity of motion. If in addition of being geometrically similar, the velocities at corresponding points are in fixed ratio, then kinematic similarity is said to be observed.

Dynamic similarity represents similarity of forces. Dynamic similarity is observed between two systems, when the magnitude of forces at corresponding locations is in a fixed ratio.

For non-isothermal systems **thermal similarity** is important. It implies that the rate of heat transfer by various mechanisms must be in matching ratios for both model and prototype.

Chemical similarity concerns the establishment of the necessary conditions in the model, so that the rate of chemical reaction at any location is proportional to the same reaction at the corresponding time and point in the prototype.

As mentioned earlier that for physical modeling of any system, the system should be realistically represented by the model. As such it has to fulfill similarity criteria. Since hydrodynamic studies of melt flows in the tundish are often not concerned with thermal and chemical similarity effects, the equivalence between a model tundish and the prototype can adequately be described via geometric and dynamic similarity [23].

In any system a balance among the various forces acting on a fluid element can be expressed by the Navier-Stokes equation [2]. For single phase, three-dimensional flows under steady state, isothermal, laminar flow conditions, the momentum balance on an elementary volume of liquid can be expressed in tensorial notation as [4, 2] :

$$\frac{\partial}{\partial x_j}(\rho u_i u_j) = -\frac{\partial p}{\partial x_i} + \frac{\partial}{\partial x_j}\left(\mu \frac{\partial u_i}{\partial x_j}\right) + \rho g_i \quad \ldots\ldots (1)$$

In corresponding dimensionless form, it is also expressed as [38] :

$$u^*.\nabla^* u^* = -\nabla^* p^* + \frac{1}{N_{\mathrm{Re}}}\nabla^{*2} u^* + \frac{1}{N_{Fr}} \quad \ldots..(2)$$

where $N_{Re} = \frac{\rho UL}{\mu} = \frac{Inertial\ force}{Viscous\ force}$

$$N_{Fr} = \frac{U^2}{gL} = \frac{Inertial\ force}{Gravitational\ force}$$

Equation (2) is the key for dynamic similarity between two geometrically similar systems. Provided these dimensionless numbers can be kept constant between model and prototype, dynamic similarity can be achieved.

As mentioned earlier, geometrical similarity means dimensional correspondence of the prototype and model tundish. Beyond this, geometrical similarity requires that the depth of the liquid in the model and the prototype must also correspond. ($H_{model} / H_{prototype} = L_{model} / L_{prototype} = \lambda$). However, at steady state the bath depth is a function of liquid flow rate through the inlet shroud and outlet nozzle[39]. In order to maintain similarity in depth of liquid, the relationship between the velocities and hence the inlet flow rate of the fluid in the model and in the prototype is to be obtained by following either of Froude similarity or Reynolds similarity. As steel flow in the tundish is gravity driven, it is understood that flow inside tundish is Froude criteria dominated. So most reduced scale-modeling studies were done mainly based on Froude similarity criteria [4].

In their study Mazumdar & co-workers [20] showed that geometric similarity necessitates that the inflow rate of water in the model be related to the inflow rate of prototype according to the relation :

$$Q_{model} = Q_{prototype}.\lambda^{5/2} .$$

They deduced this relation keeping Froude similarity criteria constant.

It is to be noted that the Froude and Reynolds similarity criteria gives the following relationships [22] :

Froude criteria : $U_{model} = \sqrt{\lambda}.U_{prototype}$

Reynolds criteria : $U_{model} = (1/\lambda).U_{prototype}$

It is clear from the above relations, that to satisfy both the criteria, the scale factor λ has to be equal to 1. In other words, only in a full-scale model can both these criteria be simultaneously satisfied.

The above derivations of relations are based on equation (1), which is valid for laminar flow conditions. In real life continuous casting tundish, the flow is turbulent. So one has to consider the equivalent momentum balance equation for turbulent conditions. For single phase, three-dimensional flows under steady state, isothermal, turbulent flow conditions, the momentum balance on an elementary volume of liquid can be expressed in tensorial notation as [4, 2]

$$\frac{\partial}{\partial x_j}(\rho u_i u_j) = -\frac{\partial p}{\partial x_i} + \frac{\partial}{\partial x_j}\left(\mu_{eff}\frac{\partial u_i}{\partial x_j}\right) + \rho g_i \quad \ldots\ldots (3)$$

In corresponding dimensionless form, it can also be expressed as:

$$u^*.\nabla^* u^* = -\nabla^* p^* + \frac{1}{N_{\mathrm{Re},t}}\nabla^{*2} u^* + \frac{1}{N_{Fr}} \quad \ldots\ldots\ldots\ldots (4)$$

Here $N_{\mathrm{Re},t} = \dfrac{\rho U L_c}{\mu_{eff}}$ the turbulent Reynolds number.

As can be seen, the only difference between equations (1) and (3), is the viscosity term (μ_{eff}). Here the viscosity is the effective viscosity, which is defined as [22] :

$\mu_{eff} = \mu + \mu_{turb}$, the summation of laminar and turbulent viscosity. The notable point is that the laminar viscosity is the property of the fluid, whereas the turbulent viscosity depends upon the flow.

According to Sahai & Burval [22], flow similarity in two isothermal tundishes can only be maintained if geometric similarity and the same value of turbulent Reynolds numbers are maintained.

But Singh & Koria [28, 29], in their experimental and mathematical study, and also reviewing the results of many other investigators, noted that the difference in Reynolds number (turbulent) for model tundish and the prototype did not show any significant influence on the resulting fluid flow pattern and RTD. They explained this behavior on the basis of turbulence theory. In their review Mazumdar & Guthrie [4] also mentioned that

under turbulent flow conditions, the turbulent Reynolds number, $N_{Re,t}$, in different tundishes, irrespective to their geometry and dimensions, are very similar.

In actual casting practices, the conditions are rarely iso-thermal. There is always heat loss through the tudish walls and melt surface. So the temperature of the incoming steel is different from the existing and out going liquid. This slight change in temperature can produce significant thermal convection. So according to Joo and Guthrie [32, 33, 34], we must include a buoyancy term in Navier-Stokes equation, in the direct numerical CFD simulations of flows in real systems. Damle & Sahai [25] later addressed this issue through dimensional analysis. They defined dimensionless velocity, length, density, pressure, time, temperature as :

velocity, $u^* = \frac{u}{U}$

length, $x_i^* = \frac{x_i}{L}$

density, $\rho^* = \frac{\rho}{\rho_{ref}}$

pressure, $p^* = \frac{p - p_{ref}}{\rho_{ref} U^2}$

time, $t^* = \frac{tU}{L}$

temperature, $T^* = \frac{T - T_0}{T_{inlet} - T_0} = \frac{T - T_0}{\Delta T_0}$

Then the Navier-Stokes equation can be written in dimensionless form as:

$$\frac{\partial(\rho^* u_i^*)}{\partial t^*} + \frac{\partial(\rho^* u_i^* u_j^*)}{\partial x_j^*} = \frac{\partial}{\partial x_j^*}\left[\frac{\mu_{eff}}{\rho_{ref} UL}\left(\frac{\partial u_i^*}{\partial x_j^*} + \frac{\partial u_j^*}{\partial x_i^*}\right)\right] - \frac{\partial p^*}{\partial x_i^*} - \frac{\beta \Delta T L}{U^2} g_i$$

$\frac{1}{\mathrm{Re}_t} = \frac{\mu_{eff}}{\rho_{ref} UL}$ where μ_{eff} = effective viscosity and ρ_{ref} =some reference density.

$$\text{Tu} = \frac{Gr}{\text{Re}^2} = \frac{\beta \Delta T_o L g_t}{U^2} = \frac{Bouyancy\ \ force}{Inertial\ \ force}$$

Where Gr is the thermal Grashof number & β is coefficient of thermal expansion.

By keeping Tu constant between model and prototype, dynamic similarity in non-isothermal system can be achieved.Examining experimental results for different tundish sizes, Damle & Sahai [25] got good agreement with their predictions. According to them the fluid flow in two different systems can be similar if the solutions of those dimensionless equations are identical.

More recently some researchers [15, 16, 35] have studied non-isothermal tundish modeling. Apart from modeling using Froude similarity criteria, ie. keeping Froude number identical for model and the prototype, they also kept Tundish Richardson number identical. So for non-isothermal tundish modeling, which they termed as thermal stratification, $\text{Tu}_{\text{model}} = \text{Tu}_{\text{prototype}}$.

Hence, $$\frac{\beta_{model} \Delta T_{model} L_{model} g}{U^2_{model}} = \frac{\beta_{prototype} \Delta T_{prototype} L_{prototype} g}{U^2_{prototype}}$$

So for model and prototype having same Froude number,

$$\Delta T_{model} = \frac{\beta_{prototype}}{\beta_{model}} \Delta T_{prototype} \ .$$

So Wen & co-workers [35], for temperature difference of liquid steel between injection spot of the ladle and the lowest temperature in the tundish, ie. at the outlet, of 15~25^0 C, corresponding temperature difference in the model, they kept was 10.75.

For calculating density (ρ) of water and of steel, at different temperatures they[15, 16, 35, 25] used the relations,

$\rho_{water} = 654.619 + 2.5446T - 0.004683T^2$ (T in Kelvin) [valid in the range 0-50^{0}C]

$\rho_{steel} = 7010.0 - 0.833(T - 1808.0)$ (T in Kelvin)

and β was calculated using relation: $\beta = -\frac{1}{\rho_{ref}} \left(\frac{\partial \rho}{\partial T} \right)_p$.

The calculated values of β for steel was 1.27 X 10^{-4} K^{-1} and that for water was 2.95 X 10^{-4} K^{-1}. Wen & co-workers [35] and Corona et al [16] used hot water for their study. But Zamora et al[8] used both hot and cold water for their studies.

2.2 Metallurgical performance study

As mentioned earlier, most of the time during casting, the tundish is operated at steady state. As such, it can be considered as a steady-state continuous flow reactor. To study the metallurgical performance, it is important to have a complete knowledge about what is happening inside the tundish.

This can be done in one of two ways:

1) By studying the flow characteristics of the system in terms of some defined parameters, which can give an idea of the flow behavior inside the tundish and its performance. ie. quantification of performance in terms of some defined parameters.
2) By directly measuring the flow field of the fluid, passing through the tundish, ie. the complete velocity distribution of the fluid within the tundish.

One of the most important functions of a tundish is to float out and separate inclusion from the steel melt. For this reason many physical modeling studies had been carried out over the last two decades. Though inclusion float out in a real continuous casting tundish cannot be accurately determined from such studies, due to large difference in model and full scale system and the complex physico-chemical reactions involved in practice, useful, qualitative information can be deduced from such studies[4].

Two different experimental approaches had been taken to quantify this metallurgical performance, ie. inclusion float out :

a) Measurement of residence time distribution to indirectly predict the performance.
b) Direct measurement of inclusion separation , using aqueous system and thus predicting the same for real system.

2.2.1 Residence time distribution (RTD)

From the Figure (1.01) it is evident that, in the process of transferring steel from the ladle to the moulds, liquid steel remains for a significant fraction of time within the

tundish. This 'dwell time' fraction is called the **'nominal'** or **'mean residence time'**($\bar{t}$). It is defined as the ratio of volume of the liquid in the reactor to the volumetric flow rate [2,4].

$$\bar{t} = \frac{V}{v}$$ where V = volume of liquid in tundish

v = volumetric flow rate of liquid into or out of tundish.

It is generally ~ 10 min or so for industrial caster tundishes [4]. So the tundish provides an excellent site for different metal processing operations.

To asses the significance of residence time and interpret the result of residence determination, the analysis of characteristics of flow inside tundish is very important.

An ideal steady–state continuous flow reactor is characterized by two extreme flow possibilities. Namely **'Plug flow'** or **'Piston flow'** or **'Linear'** reactor, and the **'Well-mixed'** or **'Backmix'** reactor [1].

According to Levenspiel [1] a **'Plug flow reactor'** is characterized by the fact that the flow of fluid through a plug flow reactor is orderly, with no element of fluid overtaking or mixing with any other element ahead or behind. There may be lateral mixing or diffusion along the flow path. The necessary and sufficient condition for **'Plug Flow'** is for the residence time in the reactor to be the same for all elements of fluid. This can be depicted in other ways1as a flow in which each element of the entering fluid moves through the reactor with a uniform velocity. On the other hand the **'Well-mixed'** reactor is a reactor, in which the contents are well stirred and uniform throughout. As such,the exit stream from this reactor has the same composition as the fluid inside [3].

But in real reactors like a **'tundish'** , the flow is in between these two extreme types. It is observed that, some of the flow entering the vessel short-circuits in a plug flow mode and goes straight to the exit. Some other tundishes have more of 'Well-mixed' flow character. Other fluid elements at the corner of a reactor hardly move and can stay for a longer time. This portion is called the **'Dead Volume'.**

The dead volume is defined that volume of the fluid, which stays within the reactor longer than **twice** the **'nominal'** or **'mean' residence time.**

Thus the reactors volume can be expressed as [1]:

$V = V_m + V_p + V_d$ Where V_m = mixed volume

V_p = plug volume

V_d = dead volume.

RTD characteristics are generally measured experimentally using stimulus-response techniques. In this technique, a tracer is added to the system and the response to this stimulus is recorded online. This recording can include colorimetry, conductimetry and spectrophotometry. Generally an appropriate (instantaneous input or step input) tracer is injected into the liquid passing through ladle shroud at time t = 0. The concentration of the added tracer is monitored continuously at the exit nozzles via one of the above-mentioned techniques. A variation of exit concentration as a function of time is obtained. Which if plotted gives a typical curve, known as 'C' curve for a pulse, or instantaneous addition and 'F' curve for a step, or jump, input. Generally the curves are represented in non dimensional form.(ie. non-dimensional concentration on the 'Y' axis and non-dimensional time on the 'X' axis.) The concentration is normalized on the basis of an uniform well mixed concentration value (inlet concentration) and the time is normalized with respect to theoretical residence time (defined earlier) [4]. The general nature of the RTD curves are shown in Figure 2.01 .

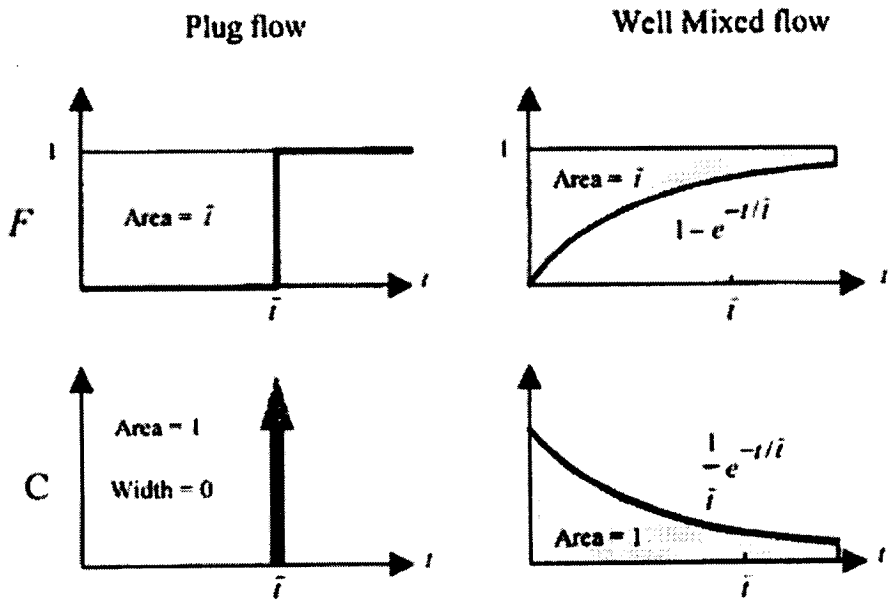

(a)

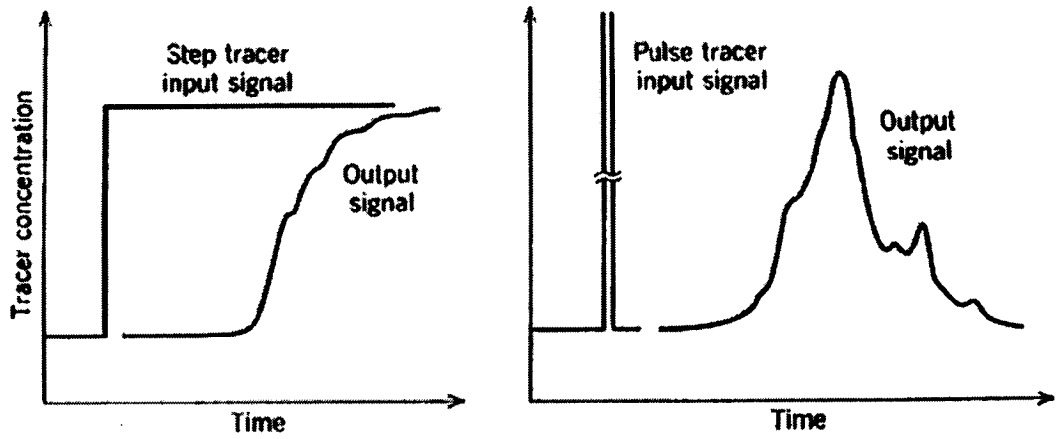

(b)

Figure 2.01: General nature of RTD curves (a) Ideal reactor [9], (b) Real reactor.[1]

Most of the researchers used 'C' curve in their studies. It has a " minimum break through time" followed by a rapid increase in concentration and subsequent near exponential decay.

From a typical 'C' curve, important RTD parameters such as minimum break through time (t_{min} or θ_{min}, the corresponding dimensionless form),the time to attain peak concentration (t_{peak} or θ_{peak}), and the average residence time (t_{av} or θ_{av})can easily be measured and used in an appropriate flow model to calculate dead volume (V_{dv}), plug volume(V_{pv}), and well-mixed volume (V_{mv}). On the basis of those estimates, inferences on the efficiencies of various transport-controlled processes in a given tundish can be made[49].

With the data obtained from RTD curves, different researchers used different models to correlate different RTD parameters. As mentioned by Mazumdar & Guthrie [4], Kemeny et al. proposed a model called a 'mixed model'. According to them:

$$V_{dv} = 1.0 - \theta_{av}$$

$$V_{pv} = \theta_{min} = \theta_{peak} \quad \}$$

$$V_{mv} = \frac{1}{C_{peak}}$$

An additional feature of that model states that the volume fractions calculated on the basis of above, should add up to unity. ie. $V_{dv} + V_{pv} + V_{mv} = 1$.

The above-mentioned model is called the 'mixed model'. The Figure 2.02a shows the 'mixed model' and the typical 'C' curve for theoretical mixed model.

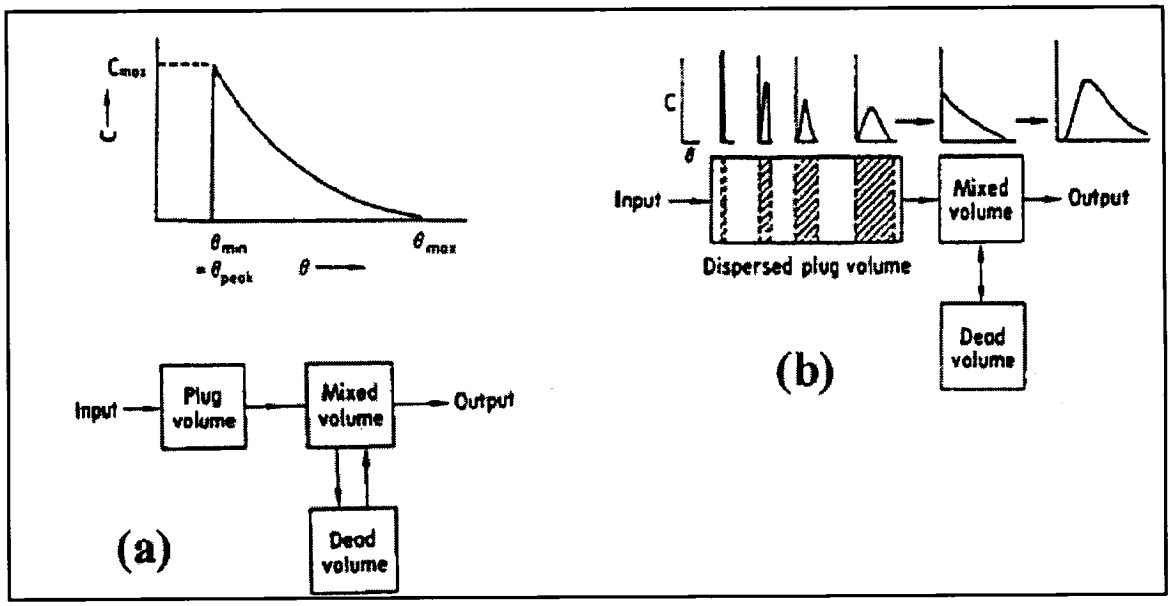

Figure 2.02: Schematic flow models and their associated theoretical flow curves [4]
(a) Mixed model, and (b) Modified mixed model

The vertical rise of tracer concentration at $\theta_{min} (= \theta_{peak})$ in the mixed model is a reflection of the existence of plug volume, where the longitudinal diffusion or mixing of dye is absent. But experimental RTD curves do not show such instantaneous increases. So $\theta_{peak} \neq \theta_{min}$. And the volume fractions calculated using the above relations do not add up to unity.

To avoid those shortcomings, Ahuja & Sahai [36] proposed 'modified mixed model'. According to them, as there is a finite time difference between the appearance of first tracer and peak concentration, there is a possibility of dispersion of tracer axially or longitudinally, before the flow exists the reactor. Instead of a plug volume, they defined, a 'dispersed plug volume' (V_{dpv}), and proposed modified form as:

$$V_{dv} = 1.0 - \theta_{av}$$

$$V_{dpv} = (\theta_{min} + \theta_{peak})/2$$

$$V_{mv} = 1 - V_{dv} - V_{dpv}$$

The Figure 2.02b shows the 'modified mixed model' and corresponding 'C' curve. As mentioned by Mazumdar & Guthrie [4], the calculation of dead volume (V_d) is a key in the calculation of different volume fractions in a tundish.

Sahai & Emi [24] in their work reviewed the issue. They showed that the error in the calculation of dead volume could lead to significant error in calculation of other volume fractions. According to them the total volume of tundish can be divided in main two parts, namely, a) Active volume (V_a), which is the combination of plug volume (V_p) and well-mixed volume (V_m) and b) Dead volume (V_d) . The dead volume may be divided in two types. In the first type, the liquid in the dead region is considered to be completely stagnant, such that the incoming liquid does not even enter in that region. Figure 2.03a shows schematically the flow through active and dead (stagnant) regions of this type.

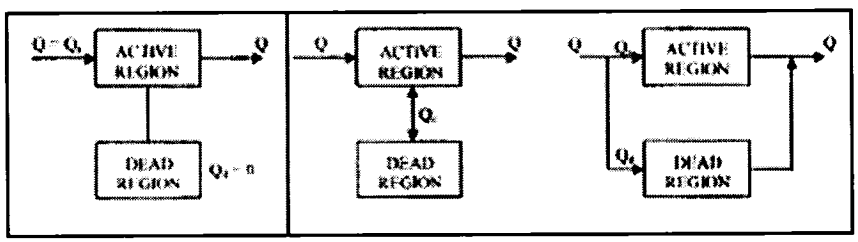

(a) (b)

Figure 2.03: Flow through active and dead regions in combined model [24]

In the second type, there is always an exchange of liquid in the dead region, with the liquid in the active zone or the liquid in the dead region move very slowly, and as a result of that some liquid stays much longer time in the tundish. This model is shown schematically in the Figure 2.03b. These two types of flow model is called a 'mixed model'.

Flow in a tundish typically falls in the second category, and is characterized by a long tail extending beyond two times the nominal residence time. Figure 2.04 shows a typical RTD curve for flow in a tundish.

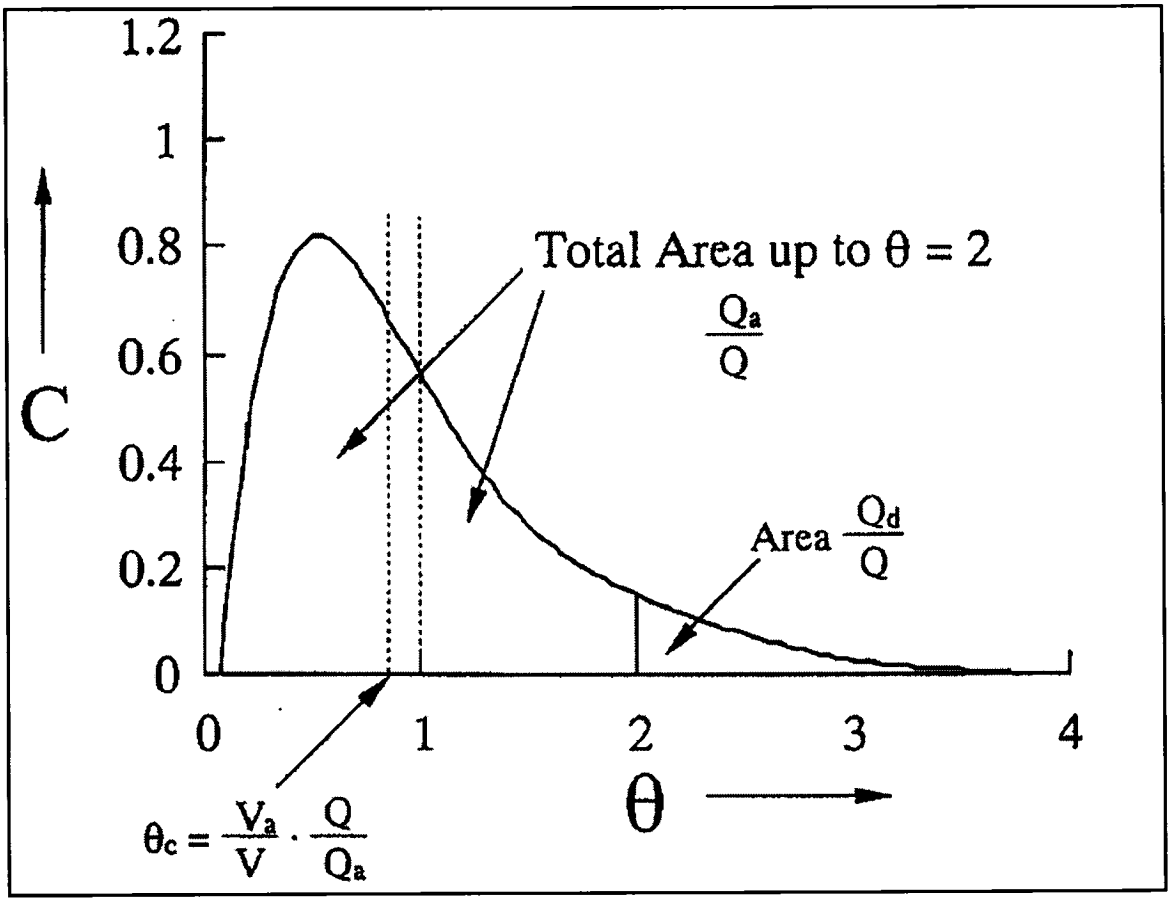

Figure 2.04: A typical residence time distribution curve for flow in tundish.[24]

Sahai & Emi [24] showed that, if the total volume of the tundish be V , then it is divided into V_a ,the active volume and V_d ,the dead volume. Similarly if Q be the total volumetric flow rate through the system, the flow rate through active and dead region be Q_a and Q_d respectively. Now the dimensionless mean time up to $\theta = 2$, be θ_c

Then $\theta_c = \frac{Measured Mean Time upto \theta = 2}{No\ minal\ Residence time} = \frac{t_c}{\bar{t}} = \frac{V_a / Q_a}{V / Q} = \frac{V_a}{V}\frac{Q}{Q_a}$

So $\frac{V_a}{V} = \frac{Q_a}{Q}.\theta_c$

Therefore, the dead volume fraction $\frac{V_d}{V} = 1 - \frac{V_a}{V} = 1 - \frac{Q_a}{Q}.\theta_c$

Sahai & Emi [24] show an example for the calculation of dead volume fraction from the experimental RTD data as below:

For the RTD curve shown in the figure 2.04,

Mean residence time for the entire curve, $\bar{\theta} = \frac{\sum_{\theta=0}^{\infty} C_i \theta_i}{\sum_{\theta=0}^{\infty} C_i}$

Mean residence time up-to $\theta = 2$, $\theta_c = \frac{\sum_{\theta=0}^{2} C_i \theta_i}{\sum_{\theta=0}^{2} C_i}$

Area under the curve up-to $\theta = 2$, $\frac{Q_a}{Q} = \sum_{\theta=0}^{2} C_i \Delta\theta$

Therefore the dead volume fraction, $\frac{V_d}{V} = 1 - \frac{Q_a}{Q} \cdot \theta_c = 1 - \left(\sum_{\theta=0}^{2} C_i \Delta\theta \right) \cdot \left(\frac{\sum_{\theta=0}^{2} C_i \theta_i}{\sum_{\theta=0}^{2} C_i} \right)$

It is interesting to note that in most of the RTD studies reported in literature, authors have used $Q_a/Q = 1$, (ie. stagnant dead volume or there is no exchange of fluid with dead region), which is practically less than 1 in real tundishes (ie. there is always an exchange of fluid with dead region, so $Q_a < Q$).

Singh & Koria [31] studied the shape of the RTD curve at length. After studying with different widths, bath heights, inlet volumetric flow rates, inlet-exit distance, exit flow control device, slag cover, submerged depth of the ladle shroud, exit flow control device (stopper rod or nozzle), tundish wall inclination, they suggested that the appearance of a single peak or two peaks in the RTD curve depends only on the width of the tundish. According to them, the probable cause for the first peak in a double peak RTD curve is short-circuiting (the straight movement of the fluid towards the exit) of the fraction of the flow, while the other peak is due to the movement of the remaining tracer. As the tundish width decreases, the longitudinal sidewalls retard the straight movement of the fluid and at a critical width the sidewalls force the portion of the short-circuiting fluid towards the middle of the tundish, where it mixes with rest of the fluid. So below that critical width, the RTD curve does not show double peak. The figure 2.05 shows the variation of shape of 'C' curves in a water model of their study.

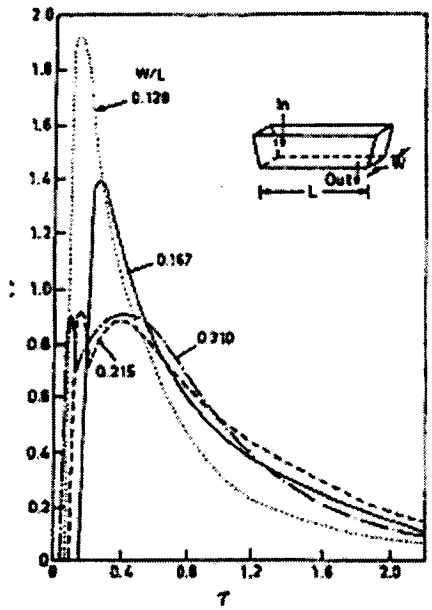

Figure 2.05: Experimentally measured C curves in a water model of single strand slab casting tundish system at various values of the dimensionless tundish width [4].

As mentioned previously, inclusion removal is one of the prime functions of the tundish. Many researchers, as mentioned by Mazumdar and Guthrie [4] have tried to study the correlation of the RTD parameters with successful inclusion removal. According to Ahuja & Sahai [36], surface directed fluid streamlines give a net upward velocity to the inclusions and hence the opportunity for the top slag layer to absorb the inclusion from the molten steel. Some important characteristics of tundish flow which would help to achieve better performance of the tundish with respect to inclusion separation and float out and other functions are [4, 36]:

1) Minimum spread of residence time.
2) Minimum dead volume.
3) Large ratio of plug to dead volume and relatively large ratio of plug to mixed volume.
4) Surface directed flow.
5) Quiescent slag layer.
6) Maximum average residence time.
7) Contained regions of mixing.

It is seen that tundish without any flow control devices cannot meet many of the above mentioned requirements. So extensive physical modeling studies had been done to investigate RTD parameters using different types of flow control devices. Most of the earlier studies were done using the weirs (as mentioned in [4] : a partial dam, covering the complete width of the tundish and extending from above the liquid pool surface to a level above the bottom of the tundish allowing liquid to flow underneath) and the dams (as mentioned in [4] : a partial dam covering the complete width of the tundish to a level below the surface of the liquid, allowing liquid to flow over it). It was observed that though weirs can ensure a quiescent slag layer, it may not eliminate short circuiting [29]. Whereas the dams can completely remove short-circuiting and promote surface directed flow and have a potential to restrict turbulence within the inlet region. The most significant influence of a dam is a marked increase in average residence time [4].

Many studies have been done using both weirs and dams [26, 29, 19]. These studies showed that a proper combination of these could create the favorable conditions mentioned earlier. According to Knoepke & Mastervich [19] and Mazumdar et al.[26] the order and number of weir and dam arrangements is also important. Whereas Koria & Singh [29] and Mazumdar et al.[26] studied the effect of the position of the weirs and dams on the RTD characteristics. Mazumdar [26] et al. showed the slotted baffles with inclined holes (inclined to the horizontal in upwards direction) could give similar, or better results than the result as weir/dam arrangement.

More recently, turbulence inhibiting pouring pads, often called 'turbulence inhibitors' have also been used for study purposes. They showed better results in controlling and restraining turbulence in the inlet pouring regions than dams, weirs or baffles.

Tundish geometry also plays an important role on residence time distribution. As mentioned earlier, Singh & Koria [31] extensively studied the influence of width, depth of liquid, and distance between inlet and outlet. Investigating their result, as mentioned by Mazumdar & Guthrie [4], the inlet-outlet distance influenced the RTD parameters the most. In addition to the geometry, the pouring method also showed considerable effect on these parameters. Some researchers [16, 30], studied the effect of different types and locations of inlet streams on the RTD parameters with or without using flow modifiers. For instance

Singh and Koria [30] found that submerged stream without flow modifiers produced short-circuiting whereas the argon shrouded stream showed excessive surface directed flow. The open stream generated surface turbulence but did not produce any short-circuiting. Corona et al. [16] reported that a tundish fitted with a turbulence inhibitor and dam showed a higher plug volume and is independent of ladle shroud position.(ie. centered or off centered).

Many researchers studied the role of gas injection in conjunction with flow modifiers. In their review of both water model and plant scale trials Mazumdar & Guthrie [4] suggested that inert gas bubbling helps to reduce dead volume and thus increases the inclusion floatation. It also depends on the location of the bubblers, their number and gas flow rate. They also suggested that these parameters are not unique, and must be determined by trial and error for the specific tundish in question. In a recent study, Zamora et al [15] also reported that under isothermal conditions, gas injection at small flow rates enhances plug volume and thus increase the probability of inclusion floatation.

Singh & Koria [29, 31] studied the effect of different operating conditions on RTD parameters. They based their analysis on their experimental results and the results from previous works, in trying to obtain a correlation between RTD parameters and operating conditions. Their study showed θ_{min} and θ_{peak} are weakly related to 'nozzle Froude number' (proportional to $Fr^{-0.082}$ and $Fr^{-0.029}$) while θ_{avg} is independent of 'nozzle Froude number' (defined as U_{in}^2/gd_{noz}). Burval & Sahai [22] have reported similar findings. They also concluded that the average residence time in a tundish system is independent of Froude number. This point is difficult to comprehend as Mazumdar et al [20, 26] have shown that flow in a tundish is essentially Froude dominated.

Contradictions also exist on the influence of flow rate (throughput rate) on RTD parameters. Coulter et al [39] reported an increase in the minimum residence time, t_{min} , along with improved inclusion removal can be achieved by decreasing throughput rate, while Chiang [37] reported the opposite. Similarly the results with tundish bath height, Coulter et al [39] reported increase in minimum residence time, while Singh & Koria [31] indicated it is inversely proportional with bath height. As the detailed experimental procedures are not available in each study, it is difficult to compare the results.

Most of the earlier modeling studies reported in the literatures dealt with symmetrical two strand tundish system. The studies using multistrand tundish, both symmetrical and asymmetrical, are comparatively less in number. Both Martinez & Solis [34] and Mazumdar et al.[26] , showed there are considerable difference in RTD parameters for different strands for a multistrand tundish. They also showed that the strand dis-similarity could be minimized by using a proper flow modifier.

In studies of multiple strand tundishes, it was observed, that most of the time the RTD parameters were reported for an individual strand only. From those data, different flow volumes cannot be calculated directly for the whole tundish. Since the concepts for estimating those values from the 'C' curve, presented earlier, cannot be extrapolated for multistrand system in a straightforward manner. Mazumdar and Guthrie [4] had shown a modified procedure, for calculating performance parameters, which is as follows :

Consider a multistrand tundish with N strands operating at a constant head.

The volumetric flow rate Q through each strand is equal.

The amount of tracer flowing out in any time through any of the N strands (say 'i' th strand in a time period Δt is :

$$\Delta m_i = C_i(t) Q \Delta t$$

Similarly the corresponding fraction of material that flows out through the exit 'i' in the same period of time:

$$\frac{\Delta m_i}{M} = E_i(t)\Delta t$$

or in differential form $\frac{dm_i}{M} = E_i(t)dt$

Here M is the total mass of injected tracer and $E_i(t)[= C_i(t)Q/M]$, is residence time distribution function for the ith strand. Now expanding for i=1,2,3,...N, and integrating within limit t=0 to t= ∞, it can be shown that,

$$\int_0^\infty E_1(t)dt + \int_0^\infty E_2(t)dt + \int_0^\infty E_3(t)dt..... = 1.0$$

or, $\int_0^\infty E(t)dt = 1.0$

where E(t), the overall residence time distribution function, equal to the sum of the RTD functions of the individual strands. Based on the above procedure, a characteristic curve can readily be derived for tundish from the individual strand data. As RTD function is directly proportional to the concentration C, and since Q, M are constants, E vs t curve can readily be translated , if required to C vs t curve. Then various fractional volumes can easily be calculated as shown before.

2.2.2 Direct measurement of inclusion seperation

As mentioned earlier, the most important function of a tundish is to provide enough time for inclusions to float up. As with the best ladle metallurgy practice, the inclusion transfer into the tundish is inevitable and as it is the last vessel before solidification in moulds, steel remains in liquid state, considerable efforts had been given in research to modify the fluid flow inside tundish so as to achieve the above mentioned goal.

In a quiescent melt, U_t, the terminal rising velocity of a spherical particle depends on the Reynolds number. This terminal velocities at different Reynolds number ranges can be calculated using the relation between drag coefficient and Reynolds number. The relations at different ranges are stated as below: [7]

$f = \frac{24}{\mathrm{Re}}$ for Re < 0.1 Stokes law range

$f = \frac{18.5}{\mathrm{Re}^{3/5}}$ for range 2<Re< 5 X10^2 Intermediate law range

$f = 0.44$ for range 5X10^2 < Re < 2X 10^5 Newton's law range

Figure 2.06 shows the variation of drag coefficient with the Reynolds number in different ranges.

For some engineering purposes, as indicated by Kim [9] the Stokes law range can be extended to Re < 2. Nakajima [12] had indicated that the fraction of particles greater than 150 μm size is almost negligible. Calculating the maximum particle size in the Stokes law region as 190 μm, Ben [9] had concluded that the inclusions in molten steel generally follow Stokes law.

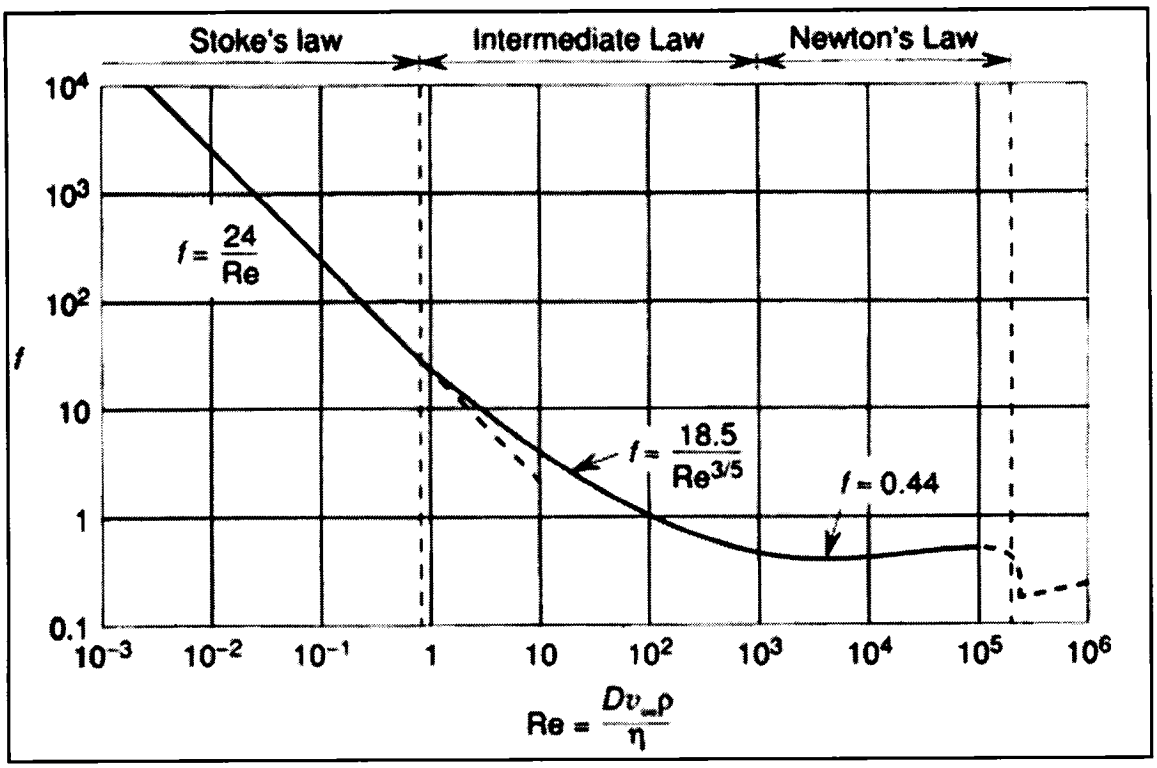

Figure 2.06: Variation of drag coefficient with Reynolds number [7].

According to Szekely & Ilegbusi [3] when the melt is in motion, the rising velocity will have to be added vectorially to both mean and fluctuating velocity components. Calculating the floating time for a small (20 μ m) and a large (100 μ m) particle, they showed that with residence time of 4 min, the bigger particle may float out, whereas the smaller would still remain in the liquid. They[3] suggested three ways to improve the situation. Namely:

1) Arrange for upward directed flow, that can carry smaller particles with it.

2) Design inlet stream in such a way that they are not carried down to the bottom but are introduced in somewhat higher level.

3) Design a way so that the particles can agglomerate and form a larger size, which can easily float out.

Shirabe & Szekely [27] proposed an equation for the rate of particle coalescence N_p as follows:

$N_p = 1.67\overline{R}^3 n_1 n_2 \left(\frac{\varepsilon}{\upsilon}\right)^{\frac{1}{2}}$ for two spherical particles.

Here $\overline{R}$ = sum of the radii of two coalescing particles

n_1 = number density of particles of 'size 1'

n_2 = number density of particles of 'size 2'

ε = rate of energy dissipation

υ = kinematic viscosity.

To study the fluid flow conditions required for floatation of nonmetallic inclusions, many researchers had studied water models using hollow glass spheres (simulating nonmetallic inclusions in steel melt). In these studies, these microspheres were introduced into the tundish in the form of a slurry via the ladle shroud, and the exit particle concentration (typically the number density or the weight) was monitored via different techniques known as, the aqueous particle sensor (APS II) based on the on-line Electric Sensing Zone (ESZ)0 [17] or the COULTER Multisizer (an off-line ESZ technique) [39].

But as mentioned by Mazumdar & Guthrie [4] this modelling of inclusion floatation can not be scaled up with the full scale steel melt on a one to one basis, still an useful insight of the process can be obtained from this modeling studies. They [4] mentioned that, some researchers (Martinez et al), using different shapes and sizes of tundish reported an increase in the removal efficiency of inclusions (~ 80 micron) with an increase in the plug volume fraction. They [4] also mentioned Plant scale trials by some researchers (Xintian et al.) confirmed this fact.

Some researchers have also tried to correlate quantitatively the amount of inclusion removal possible [expressed as residual ratio,R , $\frac{N_{out}}{N_{in}}$, ie the ratio of number of

inclusion entering into the tundish to the number of inclusion going out of tundish to mould] with the rising velocity of the inclusions.

Anticipating plug flow behavior in the tundish, S. Tanaka [11] correlated the residual ratio with rising velocity, U_t, of inclusion in the following equation:

$$R = \frac{N_{out}}{N_{in}} = \exp(-\bar{t}U_t / h)$$

here $\bar{t}$ = mean residence time & h = depth of fluid in tundish.

Dividing a real reactor in dispersed plug flow volume, backmix flow volume and dead volume, Nakajima [12] in his thesis, correlated residual ratio of inclusion with back mix flow, plug flow, fluid flow rate and rising velocity of inclusions in the following equation:

$$R = \frac{N_{out}}{N_{in}} = \left(1 + \frac{A_{dp}U_t}{\frac{A_{dp}}{A_b}.Q} \right)^{-1} * \exp\left(-\frac{A_{dp}U_t}{Q} \right)$$

here A_{dp} = surface area of dispersed plug volume

A_b = surface area of plug flow volume

Q = fluid flow rate

U_t = rising velocity.

2.3 Slag entrainment and vortex formation

Premature entrainment of any supernatant slag layer during drainage of the vessels [ladle or tundish] in a continuous casting operation is always a topic of concern for every quality conscious steel maker.

In a tundish, during casting operations, slag entrainment can occur mainly during three stages. Namely - during initial filling of tundish

- during the ladle changes
- during the last stages of casting, when the tundish is gradually emptied.

Slag entrainment can occur due to two reasons. Firstly due to mixing of slag and metal during initial filling or tundish refilling, just after a ladle change. Secondly, it can occur due to the formation of a funnel vortex during initial tundish filling, during tundish refilling at the time of a ladle change or at the last stage of the casting operation, ie when tundish is gradually emptied out.

During continuous casting at QIT, the liquid steel from the ladles are totally emptied into the tundish. The number of ladles used in one cycle can be four to ten depending on productivity. The tundishes are then totally drained at the end of each cycle. Thus, vortex formation problems will arise at the end of a cycle. However, it is also possible for vortexes to be formed over the exit nozzles during partial draining associated with ladle changes.

The slag entraining funnel can be of two types: a) vortexing funnel and b) non vortexing funnel. Though both of them have a similar funnel shape and produce similar end effects, their hydrodynamic mechanisms are completely different. For a funnel to be called vortexing, some rotational motion in the fluid is required. This is not true for the case of a non-vortexing funnel.

In the case of fluid flow in tundish during continuous casting operation, vortexing is the cause for the formation of a funnel, and hence only this category of funnels is reviewed in this section.

According to potential flow theory, the potential or free vortex is an idealized flow situation, arising from the superposition of two of the three elementary plane flow situations, namely, the line vortex and the line sink. It states that the surface streamlines of a potential vortex are logarithmic spirals and the free surface is hyperaboloidal in shape. The flow is assumed to be steady and invicid, and radial and axial velocity components in the infinitely large vessel is zero. The 'bathtub vortex' formed when water drains through a bottom hole in a tank is a good approximation of a free vortex [5]. This idea is graphically expressed in the Figure 2.07 & 2.08.

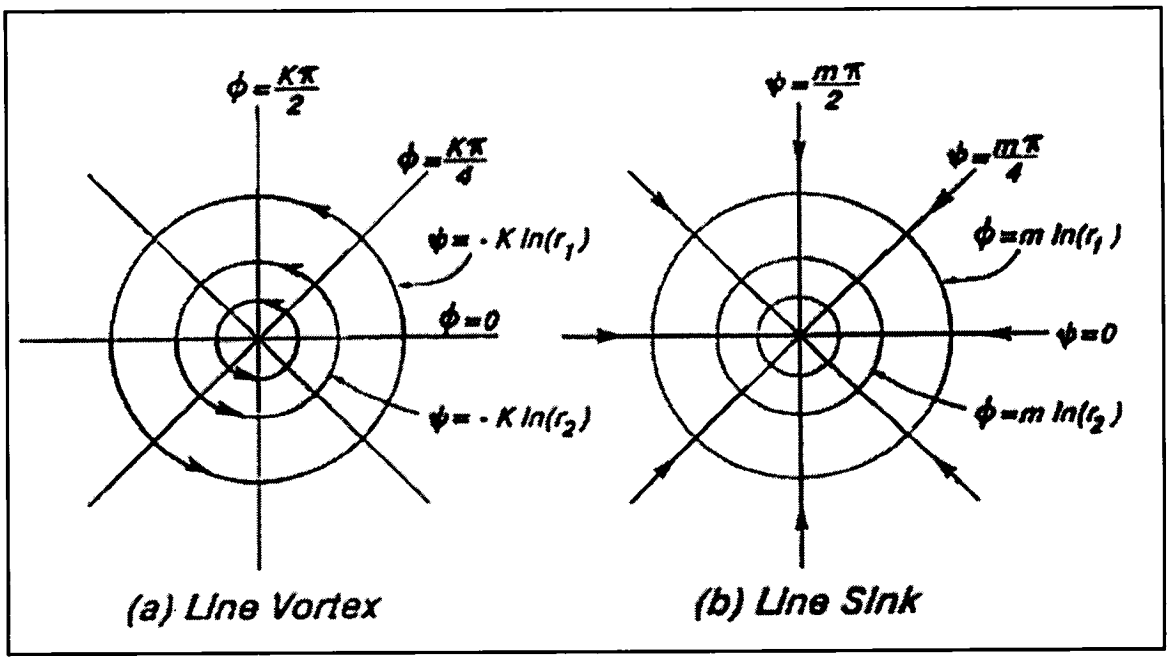

Figure 2.07: Graphical representations of a line sink and line vortex.[9]

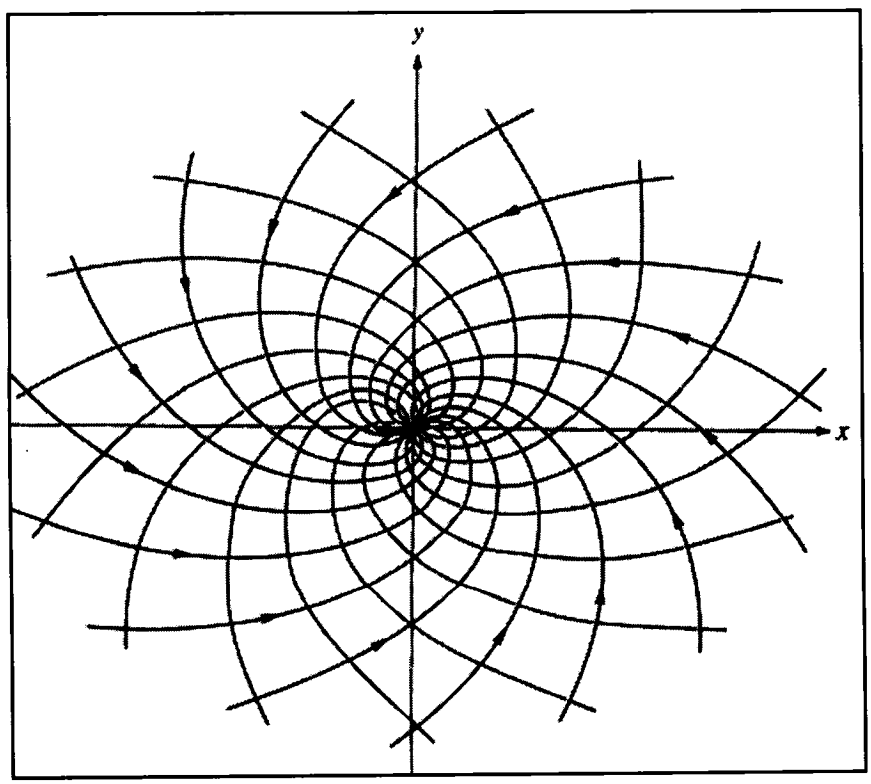

Figure 2.08: Streamlines for a vortex plus sink [5]

Based on the principle of conservation of angular momentum, the tangential velocity distribution of a free vortex can be written as [2, 5]

$V_\theta = \frac{K}{r}$ where r is the radial coordinate and K is the strength of vortex.

Whereas for ideal liquid whose angular velocity , ω, is constant, is referred as forced vortex [6]

So for forced vortex $\omega = \frac{V_\theta}{r}$ = constant.

The equations for free vortex and forced vortex can be combined into a single equation as follows: [8]

V_θ = '*constant*' / r^n ,

where n = 1 for free vortex and n = -1 for forced vortex.

Most of the vortexing funnels encountered in practice have a value of n in between 1 and –1.

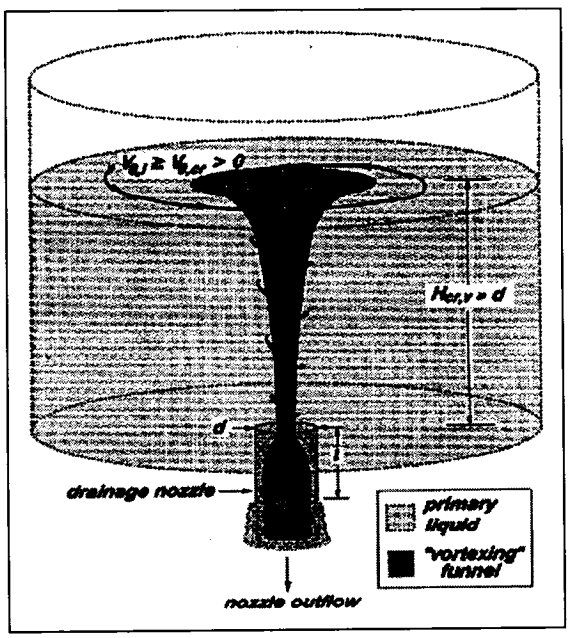

Figure 2.09: General characteristics of funnel vortex.[40]

Figure 2.09 shows the characteristic features of a vortexing funnel at its critical point for the case of teeming a cylindrical ladle through a centrally located floor nozzle. A necessary condition is that the liquid contained in the ladle should contain non-zero residual tangential velocities at the start of teeming. [40]

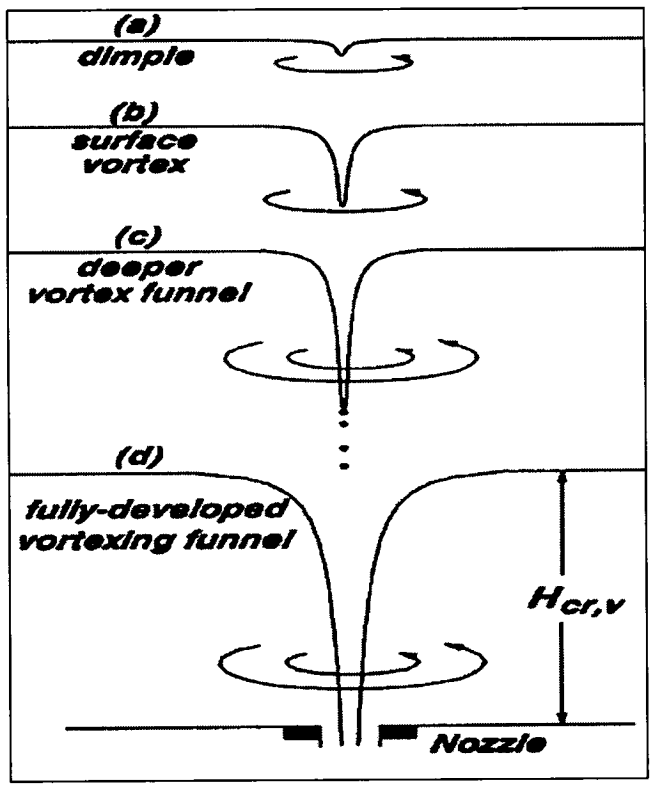

Figure 2.10: Different stages of vortex formation.[8]

In his thesis Shankaranarayanan [8] summarized the development of a vortex through different stages. These are shown in Figure 2.10. A vortex goes through four stages of development. At the first where the liquid head is very large and/or any residual tangential velocity is low, a tiny dimple is formed on the surface (Figure 2.10 a), usually centered on the axis of rotation of the tangential motion. As the liquid head decreases or the tangential velocity increases, the dimple starts extending towards the drainage nozzle, first into a tiny surface vortex (Figure 2.10b), then deeper vortex funnel whose tip shows

rapid rotation (Figure 2.10c) and finally to a fully develop vortexing funnel (Figure 2.10d) that entrains supernatant fluid. [8]

The rate of progress through the four stages itself is dependent on the residual tangential velocity and its spatial distribution in holding vessel. In the presence of strong tangential velocities, progress from dimple to the fully developed vortexing funnel is almost instantaneous. When the residual velocities are weak, the dimple takes a longer time to grow and the diameter of the funnel becomes smaller. [8] After becoming a fully developed vortexing funnel, further decrease in liquid head is accompanied by an increase in the diameter of the funnel and consequently an increase in supernatant liquid entrainment.

Apart from the study of mechanism and hydrodynamics, many researchers had studied the velocity distribution in the free vortex. Measurement showed that the tangential velocity varied with radial position alone, with very little dependence on axial position. [44] as shown in Figure 2.11.

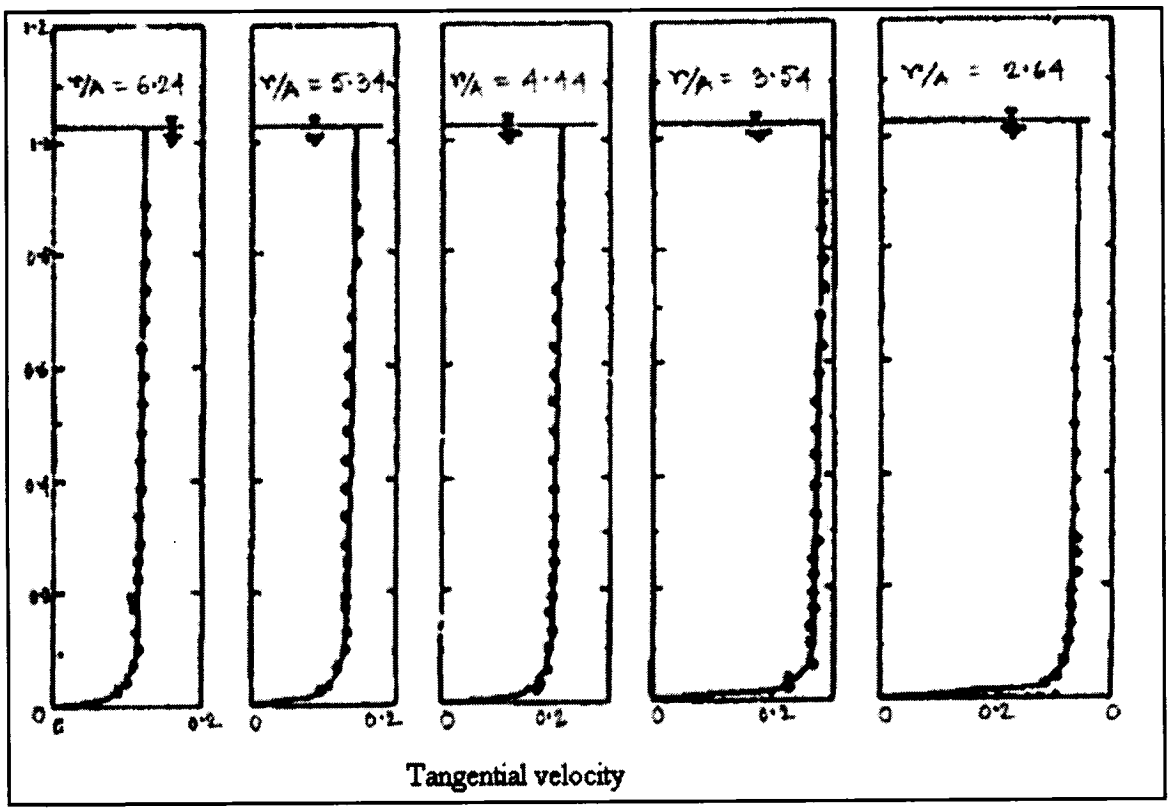

Figure 2.11: Tangential velocities (feet/sec) in the outer free vortex region at various depth and radii (feet) (A = nozzle radius)[44]

Anwar[42] also found the same trend, which is shown in Figure 2.12

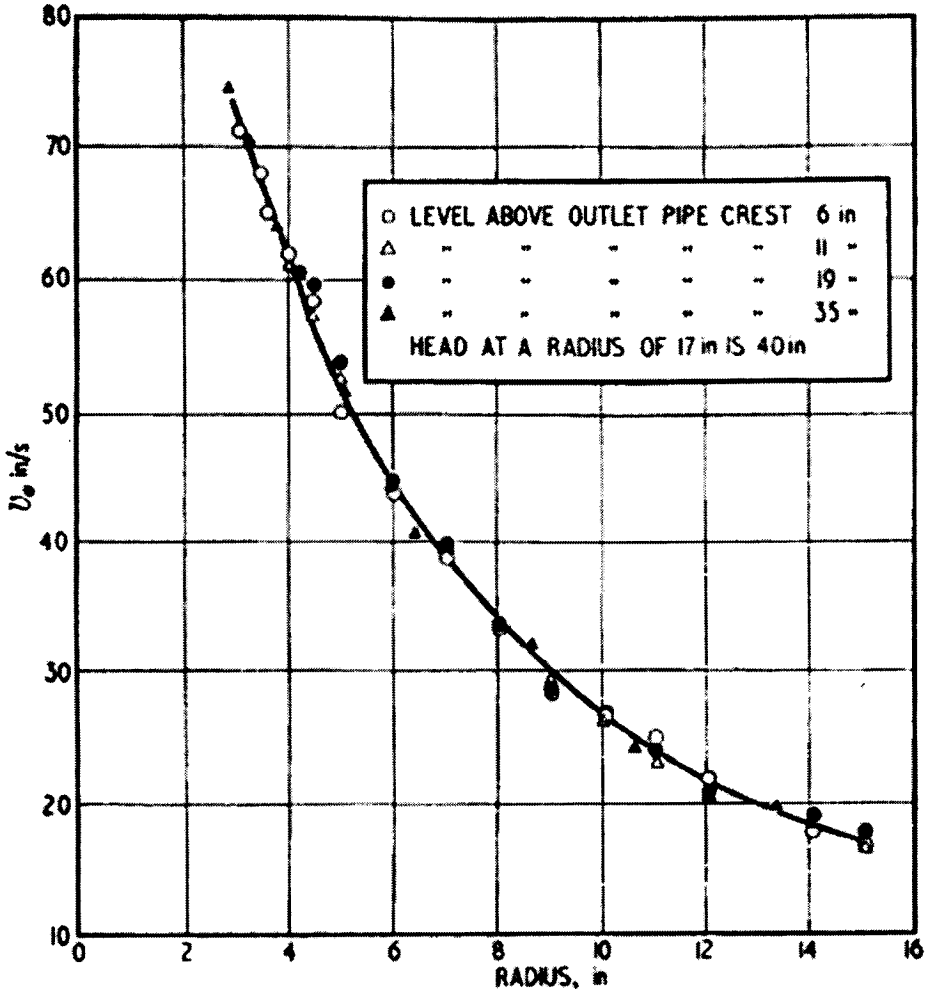

Figure 2.12: Tangential velocities(V_θ) in the outer free vortex region at different horizontal levels [42]

For the case of radial velocity distribution, Daggette & Kluegan [44] found velocities in the outer free vortex region to be higher at smaller radii and also at lower depths as shown in Figure 2.13.

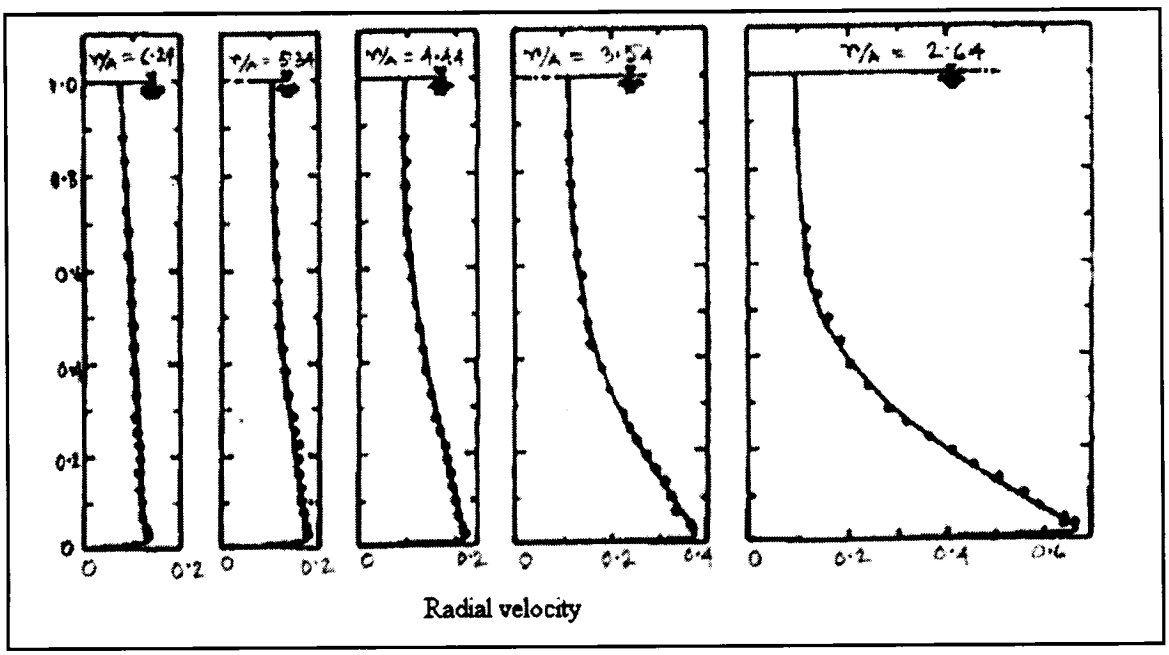

Figure 2.13: Radial velocities (feet/sec) in the outer free vortex region at different depths and radii (feet) (A = nozzle radius) [44]

Figure 2.14 shows the radial velocity distribution in horizontal plane at pipe-entrance level – tank-bottom level with outlet pipe as reported by Anwar [42]

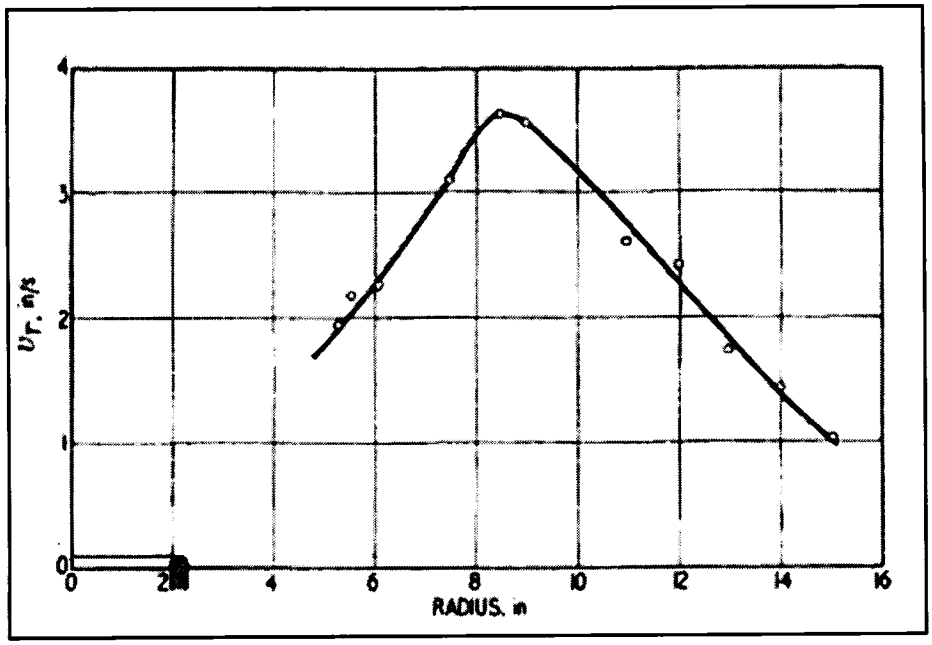

Figure 2.14: Radial velocity (V_r) distribution in horizontal plane at pipe-entrance level[42]

For the case of axial velocity, measurement showed there is a significant upward and downward velocity in the vicinity of the vortex core. Figure 2.15 shows the sketch of upward and downward axial velocities near the vortex core as proposed by Quick [41]

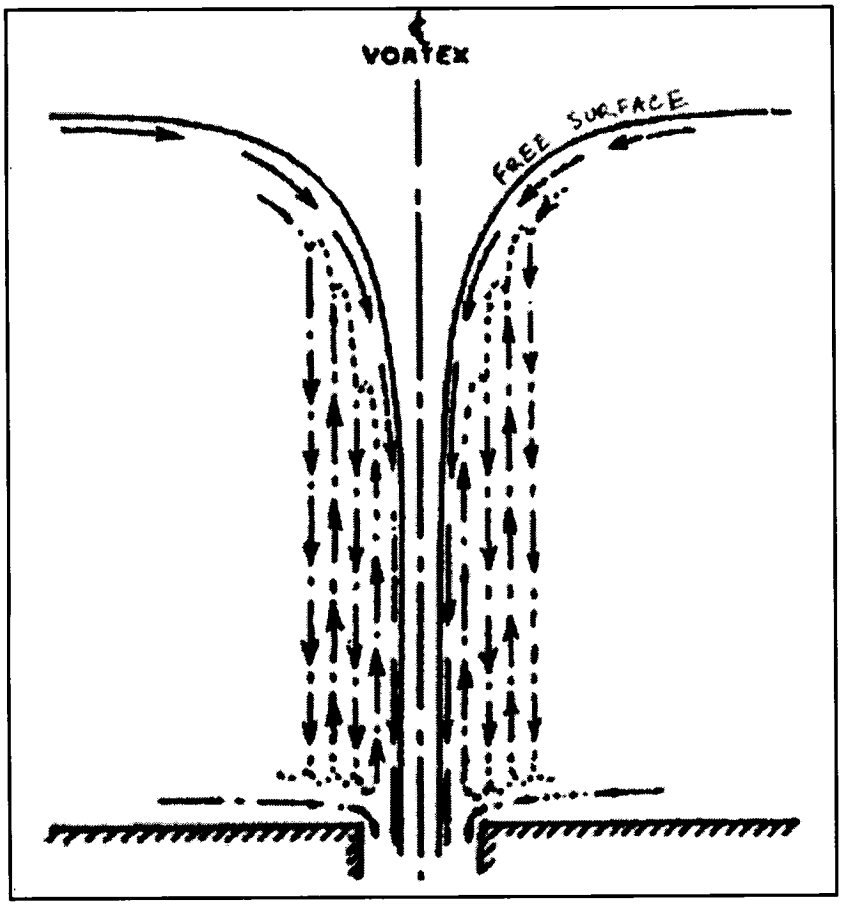

Figure 2.15: Axial velocities near vortex core. [41]

According to Kamel [43] this is inevitable when flow through the boundary layer close to the vessel floor exceeded the discharge capacity of the drainage nozzle.

Having knowledge of the dynamics and velocities of the vortexing funnels, the practice adopted industry-wide is to always maintain a sufficiently large liquid head in the tundish, to prevent any vortexing funnel formation during operation. According to Cramb et al,[13] from their study from a 1/3 hot water model, a vortex can form even when liquid head is 400-500 mm (16-18 tons) in the 28 ton Bethlehem Steel tundish (Burns Harbor tundish).

Experiments in a scale model of a one strand tundish [14] shows that $H_{Cr,v} / H_i$ increases with increasing Reynolds number. [Here Re = V_2 H_i / υ where V_2 = exit velocity from tundish, H_i = water head in tundish, υ = kinematic viscosity of water]

3.EXPERIMENTAL PROCEDURE AND SETUP

3.1 Set up

As already mentioned in section 2.1, it is only in a full-scale model that one can respect both Reynolds and Froude criteria. For this reason, a full-scale plexi glass model of 4 strand delta shaped tundish of a billet caster was used for physical modeling studies. Figure 3.01 shows the photograph of the actual full-scale model, while Figure 3.02 shows schematic top, front and side view of the model tundish.

Figure 3.01: Full-scale plexi glass model of 4-strand delta shaped tundish.

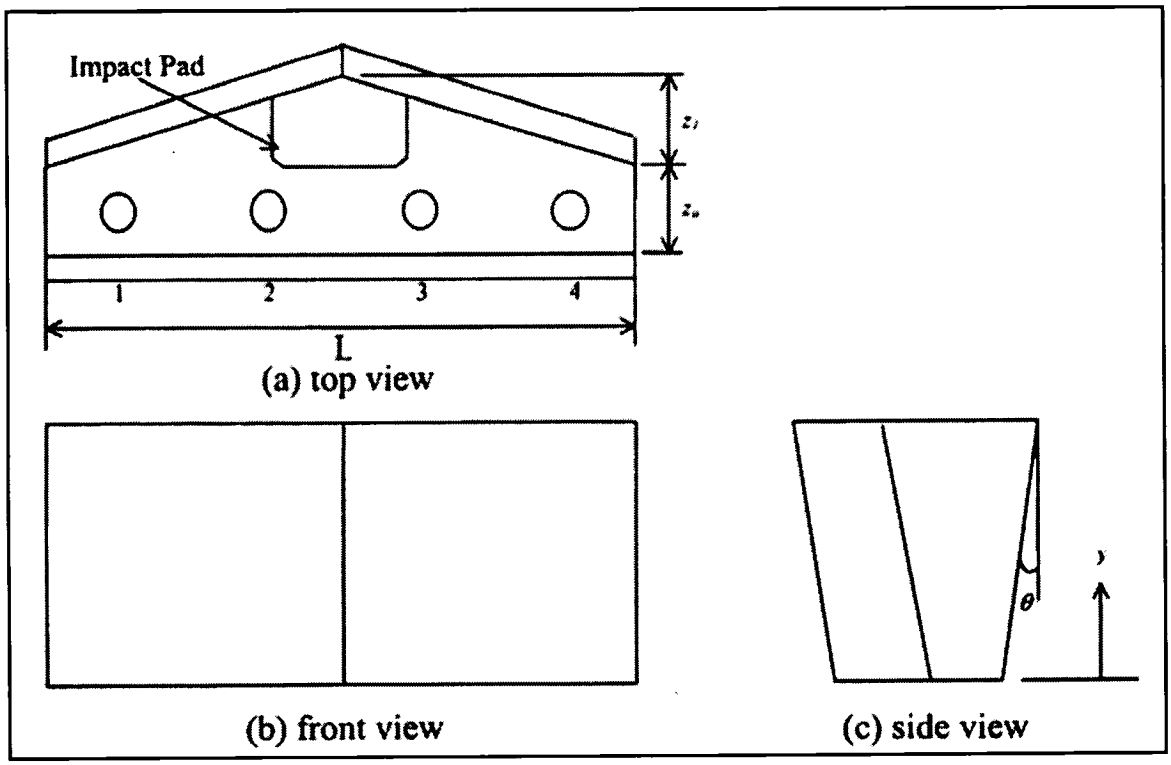

Figure 3.02: Schematic views of the model tundish.

The liquid volume in the tundish can be calculated using the relation:[9]

$$V = L.\left(z_0 + \frac{z_1}{2}\right)y + L.\tan\theta.y^2$$

here L = length of the tundish bottom

z_1 = width difference between middle and the side at tundish bottom.

z_0 = side width at tundish bottom.

θ = side wall inclination

y = level of liquid.

The tundish is fed with a rectangular top tank that is 3 m high, which can be used to simulate the flow of steel from a full ladle. Water from the tank comes into the tundish via a 'ladle' shroud, attached with a two-plate slide gate system, which controls the in-flow of water. The studies were carried out using two types of flow modifiers, namely:

1) RHI impact pad [a pad supplied by the QIT for investigation] as shown in Figure 3.03 & 3.04.
2) The standard QIT impact pad with a front lip height increased by 2 inch (~5 cm) and with side lips inclined at 45^0 , henceforth called **'Optimized QIT pad' or 'Optimized pad'.** This pad was designed by CFD analysis to give optimum performance in terms of inclusion separation. This is shown in Figure 3.05. Figure 3.06 shows the cross section of the side lip.

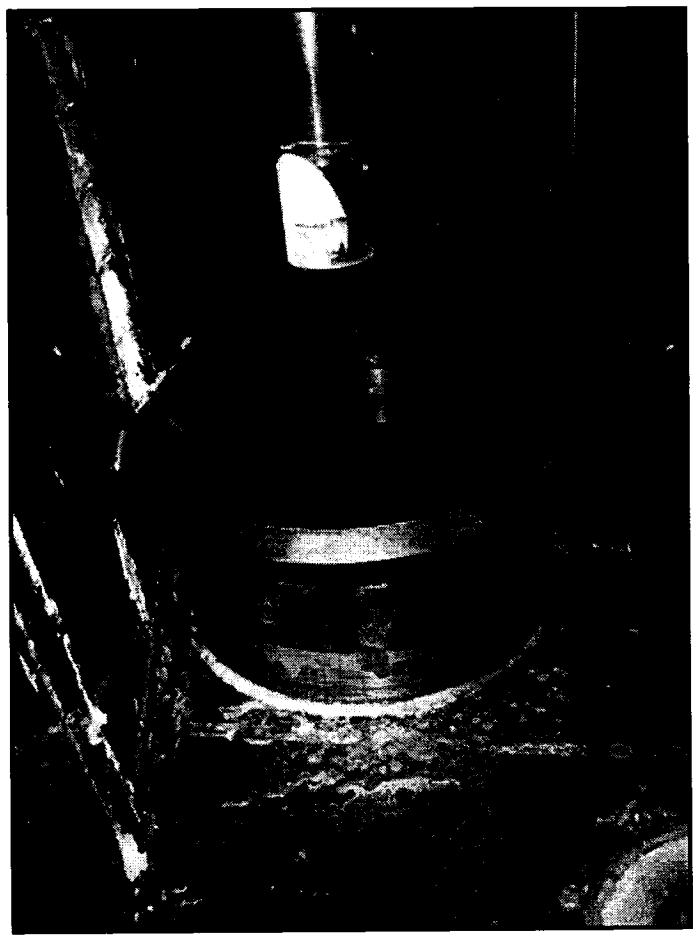

Figure 3.03: RHI pad attached in the tundish.

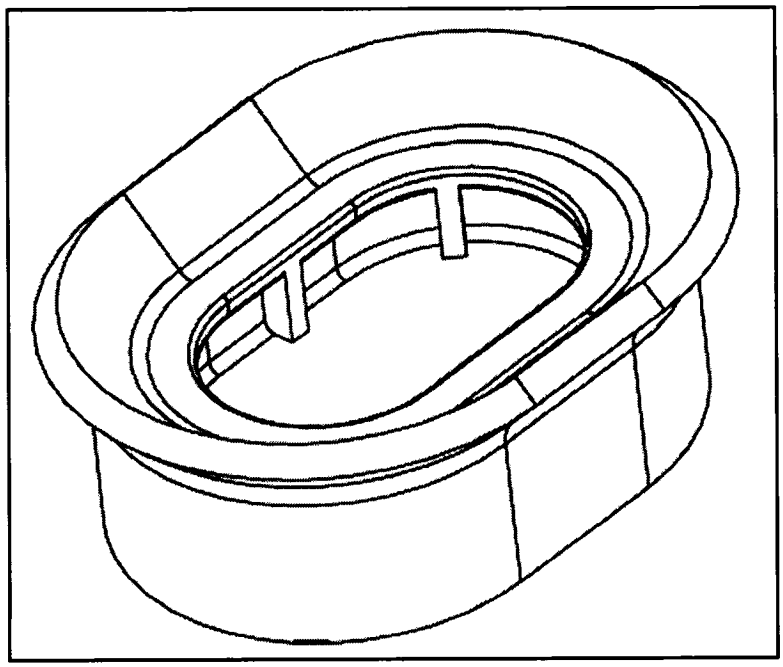

Figure 3.04: Diagram of the RHI pad .

Figure 3.05: Optimized QIT pad with 45^0 angled side lips attached in tundish.

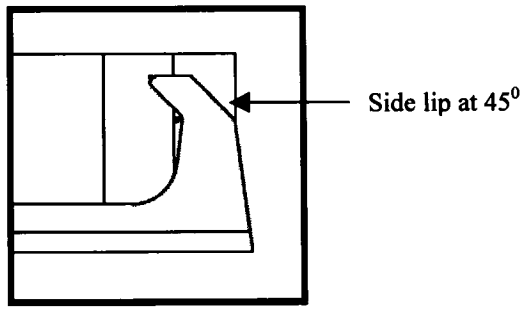

Figure 3.06: Cross section of side lip of the optimized QIT pad

Table 3.01: Physical properties of water (20^0) and liquid steel (1600^0)[49]

Property	Water (20^0C)	Steel (1600^0C)
Molecular viscosity (μ), $kg/(m.s)$	0.001	0.0064
Density (ρ), kg/m^3	1000	7014
Kinematic viscosity ($\nu = \mu/\rho$), m^2/s	10^{-6}	0.913×10^{-6}
Surface tension (σ), N/m	0.073	1.6

Table 1 above shows the properties of water at 20^0 C and steel at 1600^0 C. The most important property, the kinematic viscosity is almost the same for steel and water. This is the reason why water can be taken as modeling fluid for physical simulations.

The flow rate was maintained at 172 ± 2 L / min. and the height of water in the tundish was maintained at 50 cm level at steady state. The filled volume corresponds to approximately 12 t of steel, which is the capacity of the tundish under investigation. The submerged entry nozzle diameter was fixed at ~ 1.6 cm and the shroud inner diameter was ~ 6.0 cm, submerged inside the water by 5 cm under steady state operating conditions. These features correspond to the standard operating conditions of the real tundish.

3.2 Procedure

3.2.1 Slag entrainment

High density polyethylene beads, density ~ 935 kg/ m^3 with average size of 3.2 mm (diameter) were used to simulate the upper slag layer. Once the steady state condition was reached with 50 cm water height, the beads were spread evenly on top of the water. Inflow to the tundish was completely closed and the tundish was drained for either 5 or 3 min. Then the inflow slide gate valve was opened fully to gaining the water level up again to 50 cm. Then the inlet valve was again closed and the number of beads collected at the buckets, attached with wire mesh, at the outlets were counted. The arrangement is shown schematically in Figure 3.07. This gives a quantitative value of the degree of potential slag entrainment, which can happen in the real system. The waiting time was chosen to simulate the ladle changeover time in the plant. The inlet valve was opened completely during refilling, because it is standard practice in real operations to open the slide gate of the ladle fully in order to regain the steady state height in the tundish as quickly as possible after a ladle changing operation.

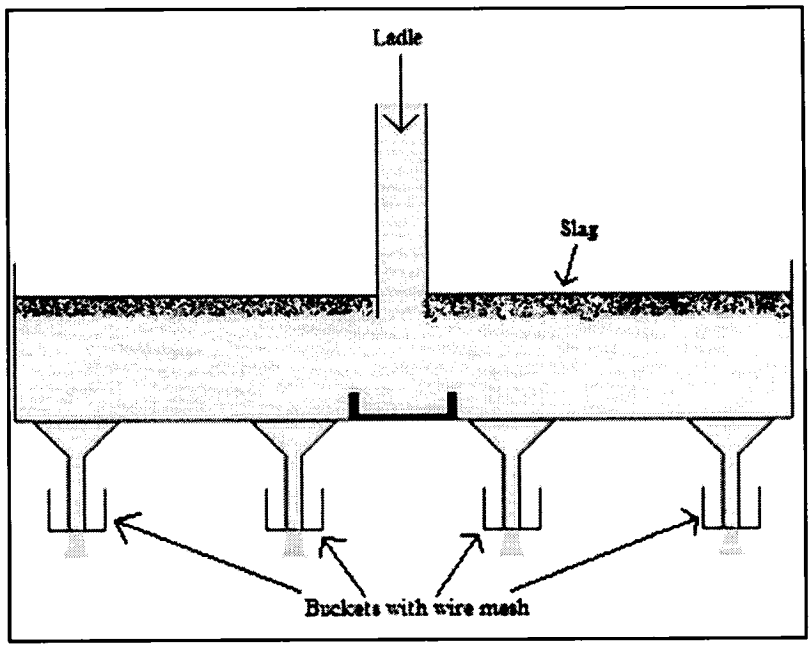

Figure 3.07: Schematic diagram of slag entrainment experimental setup

3.2.2 Vortex formation

After reaching steady state, the inflow valve was completely closed and as the liquid level dropped down, the height of the liquid at the time a stable dimple formed, was noted. Though the height of liquid when fully developed vortex is formed is somewhat lower (H_c),the dimple formation height was measured to give some extra factor of safety. Figure 3.08 shows the experimental setup for the vortex formation study.

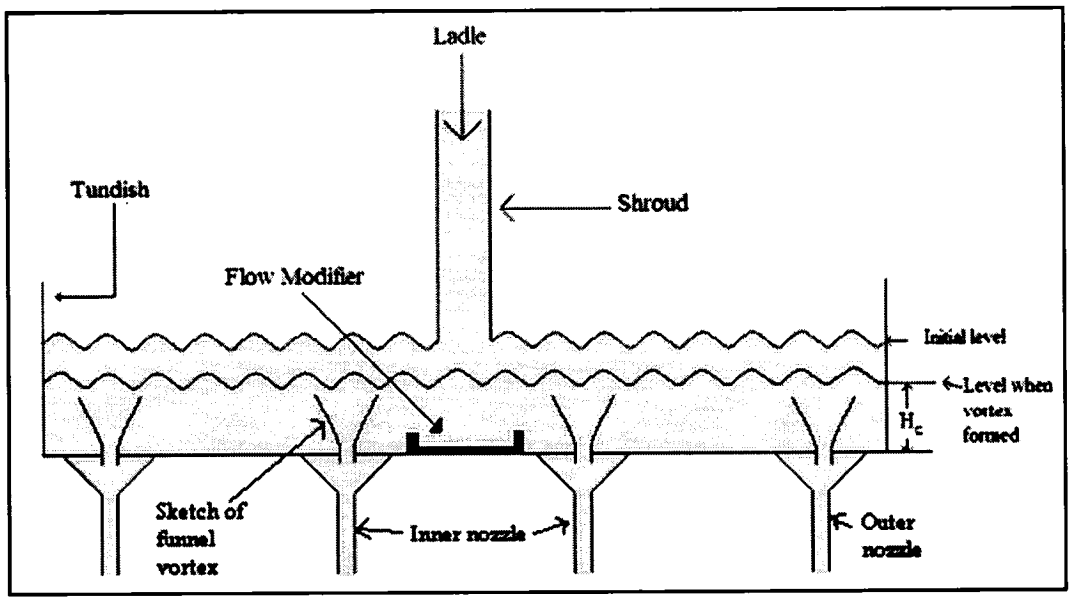

Figure 3.08: Experimental setup for vortex formation study.

3.2.3 Inclusion separation

Hollow micro spheres of sodium borosilicate glass with 5 to 150 μm were used to simulate the inclusions. A mixture of 7 litres of water and 1 litre of these micro spheres was prepared. After reaching steady state, this slurry mixture was injected into the shroud at a rate of 100ml / min. The mixture was injected for a time equal to twice the nominal residence time of the water in the tundish. Then samples of water from the outlets of the inner and outer entry nozzles were collected. The number of inclusions was measured using ESZ PAS 'Inclusion Counter' , an instrument made by **Heraeus-Electronite**, based on the electric sensing zone technique. Figure 3.09 shows the schematic experimental setup for this experiment.

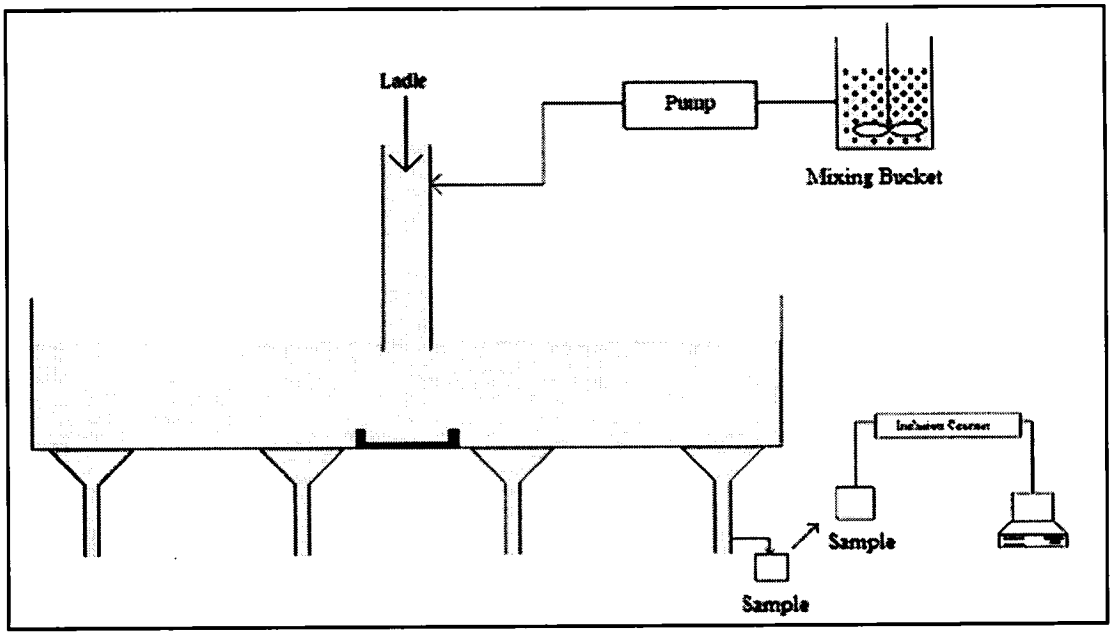

Figure 3.09: Experimental setup for inclusion separation

The apparatus and method for the measurement of inclusions is based on the technique of **LiMCA (Liquid Metal Cleanliness Analyzer)** developed at McGill University in collaboration with ALCAN. This principle is shown schematically in Figure 3.10. During inclusion measurements, the electrical current flows between two electrodes immersed in the fluid on opposite sides of an orifice in an electrically non-conductive barrier. When the non-conductive inclusions pass through the orifice, the change in electrical resistance within the ESZ, or orifice region, will generate a voltage pulse. The magnitude of the peak is proportional to particle volume. The number of peaks relates directly to the number of particles.

The size of an inclusion, d, is related to the voltage pulse, ΔV, according to the formula [46]

$$\Delta V = \frac{4I\rho d^3}{\pi D^4} \frac{1}{\left\{1 - 0.8\left(\frac{d}{D}\right)^3\right\}}$$

here ΔV : voltage pulse

I : imposed DC current

ρ : electrical resistivity of molten metal

d : particle diameter

D : orifice diameter

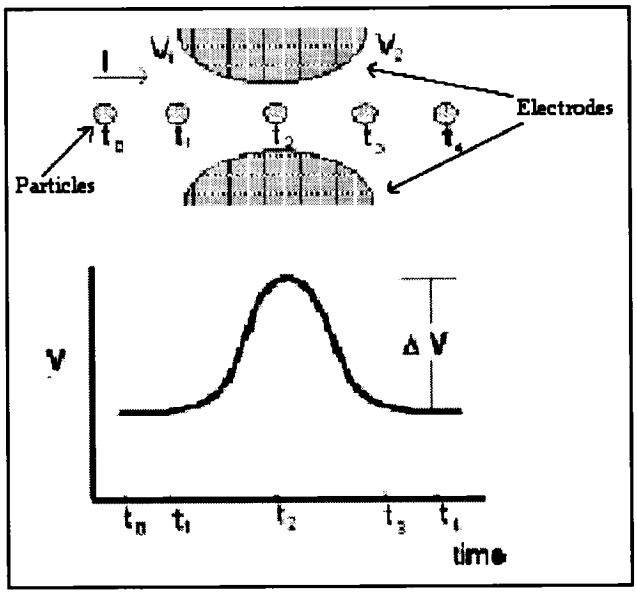

Figure 3.10: Principle of Electric Sensing Zone [46] for LIMCA

3.2.4 Residence time distribution

After achieving steady state, 400ml of concentrated sulphuric acid (0.0227 vol %) was added as tracer for pulse input. The changes in conductivity were detected at the outlets of inner and outer nozzles, using conductivity meters (100Ω Pt conductivity cell). It is provided with automatic temperature correction within 5 to 50^0 C range. These cells then convert this conductivity into a current ranging from 4 – 20 mA output. These outputs were then converted to 1-5 volts using 250 Ω resistance, in order to transfer signals to a data acquisition system that saves the signals. The ASCII files generated were then used to generate the C curve.

Figure 3.11 & 3.12 shows the calibration of the variation in voltage with acid concentration, for the two channels, which were used. Figure 3.13 shows the schematic experimental setup.

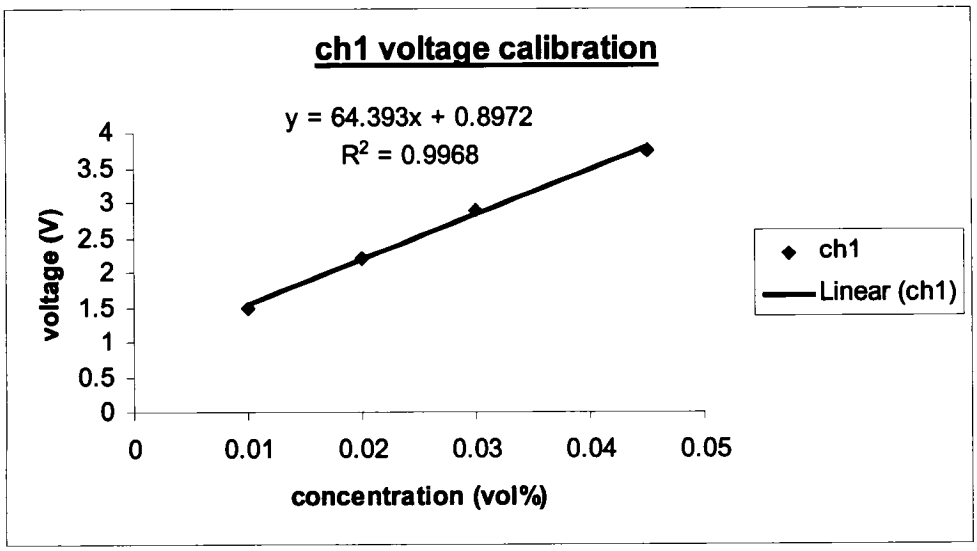

Figure 3.11: Variation of voltage with concentration for channel 1

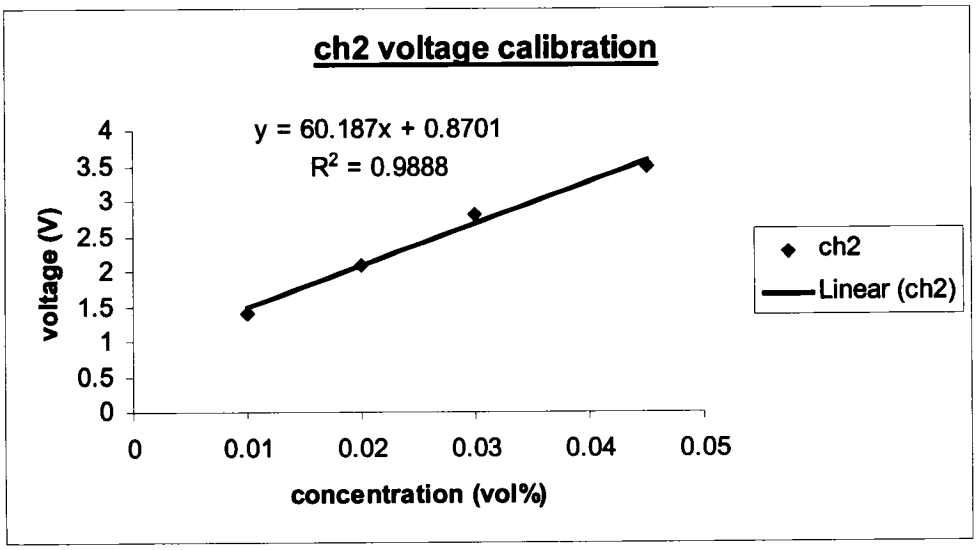

Figure 3.12: Variation of voltage with concentration for channel 2

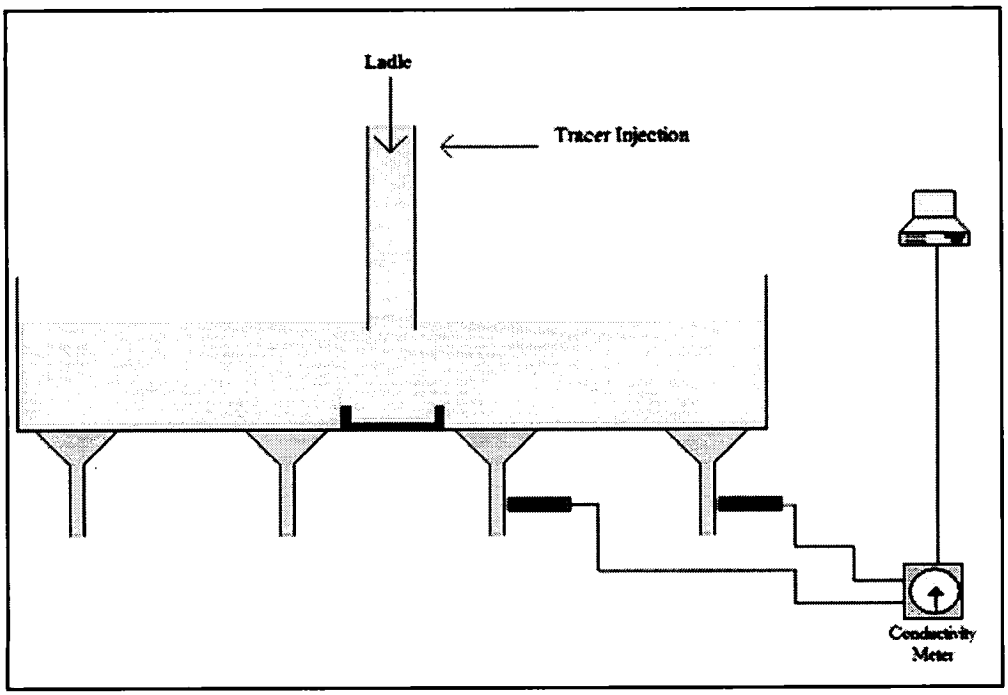

Figure 3.13: Experimental setup for RTD experiment

4. RESULTS AND DISCUSSION

4.1 Introduction

To study the performance of the tundish fitted with two different types of impact pads, four different parameters were considered, as mentioned earlier. In the constant head operation [steady state], inclusion separation ratios and residence time distributions were measured. To study the ladle changing operation vortex formation phenomena during emptying of the tundish and slag entrainment phenomena during tundish draining followed by refilling, were studied. In this section, the results of each parametric study, along with the discussions, are included under separate subheadings.

4.2 Slag entrainment

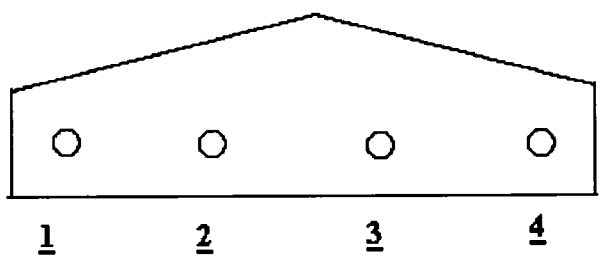

Figure 4.01: Schematic diagram of tundish to show the numbering of nozzle used in experiments.

Table 4.01: Number of beads collected during a ladle change Vs nozzle numbers (5 min draining, with RHI pad).

	Nozzle Number					
Test #	**1**	**2**	**3**	**4**	**Inner total**	**Outer total**
1	0	71	19	0	90	0
2	0	99	46	0	145	0
3	0	120	31	0	151	0
4	0	88	28	0	116	0
5	0	67	86	0	153	0
6	0	104	34	0	138	0
7	0	163	28	1	191	1
8	0	51	55	0	106	0
9	0	42	38	2	80	2
Average	**0**	**92**	**41**	**0**	**133**	**0**
Standard deviation	**0**	**37.45**	**20.08**	**0.71**	**35.09**	**0.71**

Table 4.02: Number of beads collected during a ladle change Vs nozzle numbers (3 min draining, with RHI pad).

	Nozzle Number					
Test #	**1**	**2**	**3**	**4**	**Inner total**	**Outer total**
1	0	67	54	0	121	0
2	0	95	32	0	127	0
3	0	79	19	0	98	0
4	0	62	27	0	89	0
5	0	141	40	0	181	0
6	0	80	45	0	125	0
7	0	147	51	0	198	0
8	0	189	81	0	270	0
9	0	92	57	0	149	0
Average	**0**	**89**	**34**	**0**	**123**	**0**
Standard deviation	**0**	**43.26**	**18.54**	**0**	**57.1**	**0**

Tables 4.01 & 4.02 gives the experimental results for Inner and Outer Nozzles using the RHI pad for 5 min and 3 min respectively. Water temperature was 8 –10 degree centigrade during the experiments.

Table 4.03: Number of beads collected during a ladle change Vs nozzle numbers (3 min. draining, with Optimized Pad).

	Nozzle number					
Test #	**1**	**2**	**3**	**4**	**Inner total**	**Outer total**
1	32	21	42	47	63	79
2	23	13	21	32	34	55
3	42	21	18	6	39	48
4	69	91	57	78	148	147
5	23	17	61	53	78	76
6	83	5	19	71	24	154
7	35	3	45	51	48	86
8	25	16	58	56	74	81
9	66	9	6	77	15	143
Average	**44**	**22**	**36**	**52**	**58**	**97**
Standard deviation	**22.64**	**26.75**	**20.63**	**22.97**	**40.04**	**40.57**

Table 4.04: Number of beads collected during a ladle change Vs nozzle numbers (5 min. draining, with Optimized Pad).

	Nozzle Number					
Test #	**1**	**2**	**3**	**4**	**Inner total**	**Outer total**
1	44	84	71	30	155	74
2	26	55	87	56	142	82
3	56	67	93	53	160	109
4	43	71	112	27	183	70
5	29	42	41	16	83	45
6	51	42	97	71	139	122
7	43	39	78	40	117	83
8	22	44	71	29	115	51
9	16	34	87	27	121	43
Average	**37**	**53**	**82**	**39**	**135**	**76**
Standard deviation	**13.82**	**17.19**	**20.11**	**17.7**	**29.62**	**27.39**

Table 4.03 & 4.04 gives the experimental results for Inner and Outer Nozzles using the optimized pad for 3 min and 5 min draining time respectively. (The water temperature was 22-26 degree centigrade during the experiments).

Based on the experimental results, it can be seen that the optimized impact pad caused a more even distribution in the number of beads to be collected in each of the strands, both for the 5 min and 3 min drain times during a ladle change. In other words, the results did not show any huge difference in the number of beads between the inner and outer nozzles as opposed to the case for the RHI impact pad. This may be due to a more even flow pattern inside the tundish as a result of this design of pad. The high value

of standard deviation in all the cases probably indicates the unpredictable nature of the turbulence that is generated during filling of the tundish.

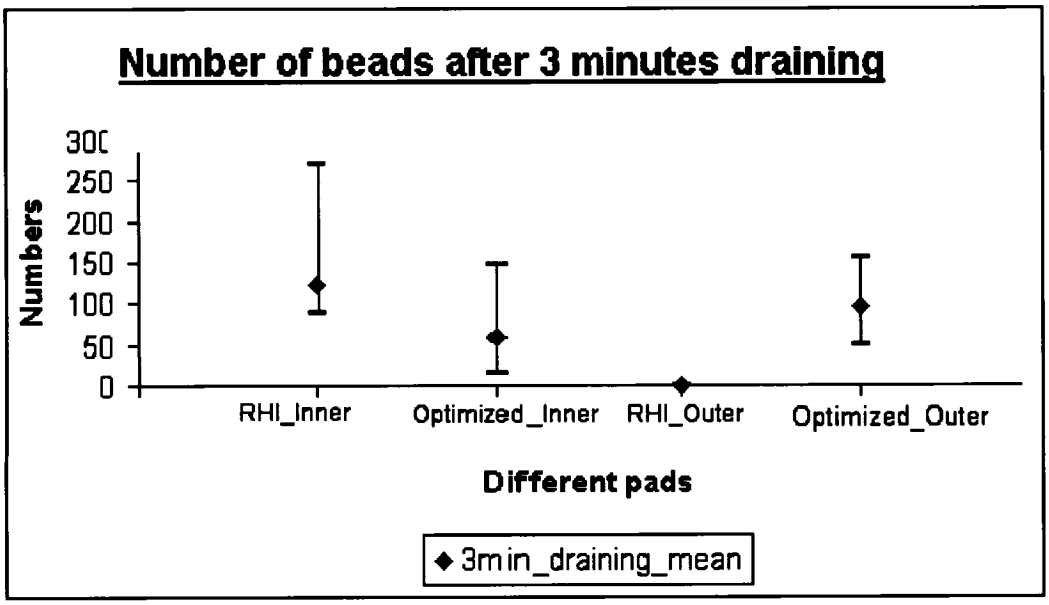

Figure 4.02: Comparative chart of collected number of beads of both inner and outer nozzles for both types of pads for 3 minutes drain time.

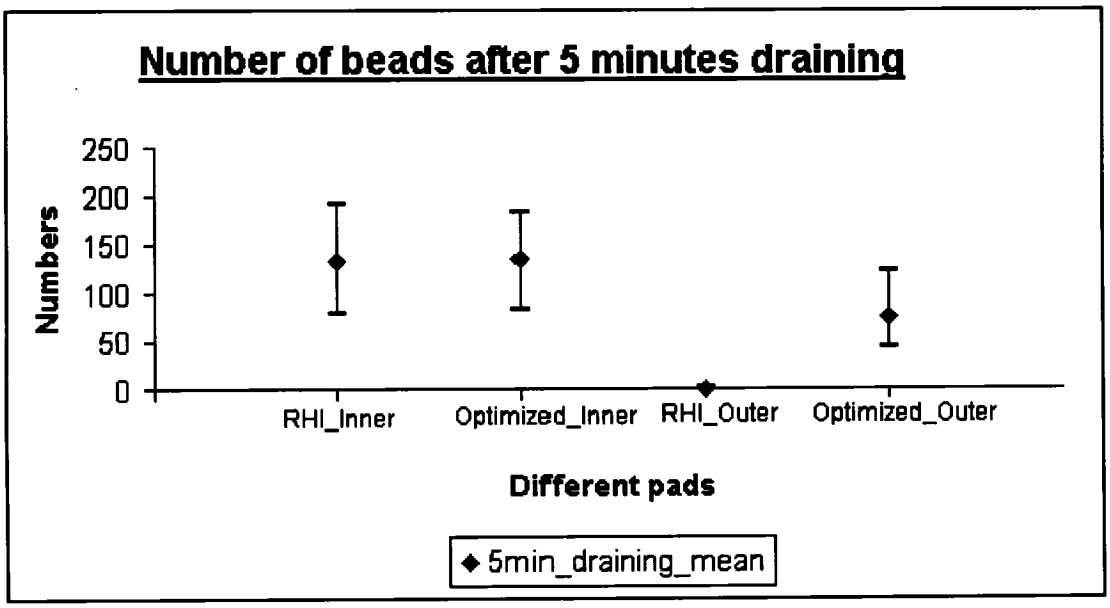

Figure 4.03: Comparative chart of number of beads collected from the inner and outer nozzles for both types of pads following 5 minutes drain time.

Figure 4.02 shows a comparative chart of the number of beads collected at the inner and outer nozzles for the RHI and QIT optimized pads for 3 minutes drain time. **Figure 4.03** provides a comparative chart of the number of beads collected at the inner and outer nozzles for the RHI and QIT optimized pads for 5 minutes drain time. In both the figures, the RHI_Outer reported zero beads. No beads being found either following 3or 5 minutes of draining.

One remarkable point was that the outer nozzles 1&4 showed more slag entrainment than did the inner nozzles, 2&3 for 3 minutes draining. Generally, the outer nozzles are expected to show less entrainment than the inner nozzles, since the fluid elements are expected to spend more time in the tundish before reaching the outer nozzles, giving more chance for slag droplets to float out. However, the present impact pad was designed to give similar residence times, but probably in this case the inside flow pattern is so modified by this impact pad that the outer nozzles have a slightly shorter residence time than the inner one, resulting in more beads draining into the outer nozzle. By contrast for 5 minute draining, the inner nozzles showed a higher entrainment of slag particles (beads). This is probably due to the level of water in the tundish at the time of reopening of the ladle shroud. For the 5-minute draining period, the water level is much lower than that following 3 minutes of draining. As a result of profuse emulsification in the region where the new incoming jet of liquid penetrates the fluid surface in the tundish, near to the inner nozzles, together with the much lower level of water within the tundish, turbulence outweighs everything, leading to more slag entrainment after a 5 minute drain period.

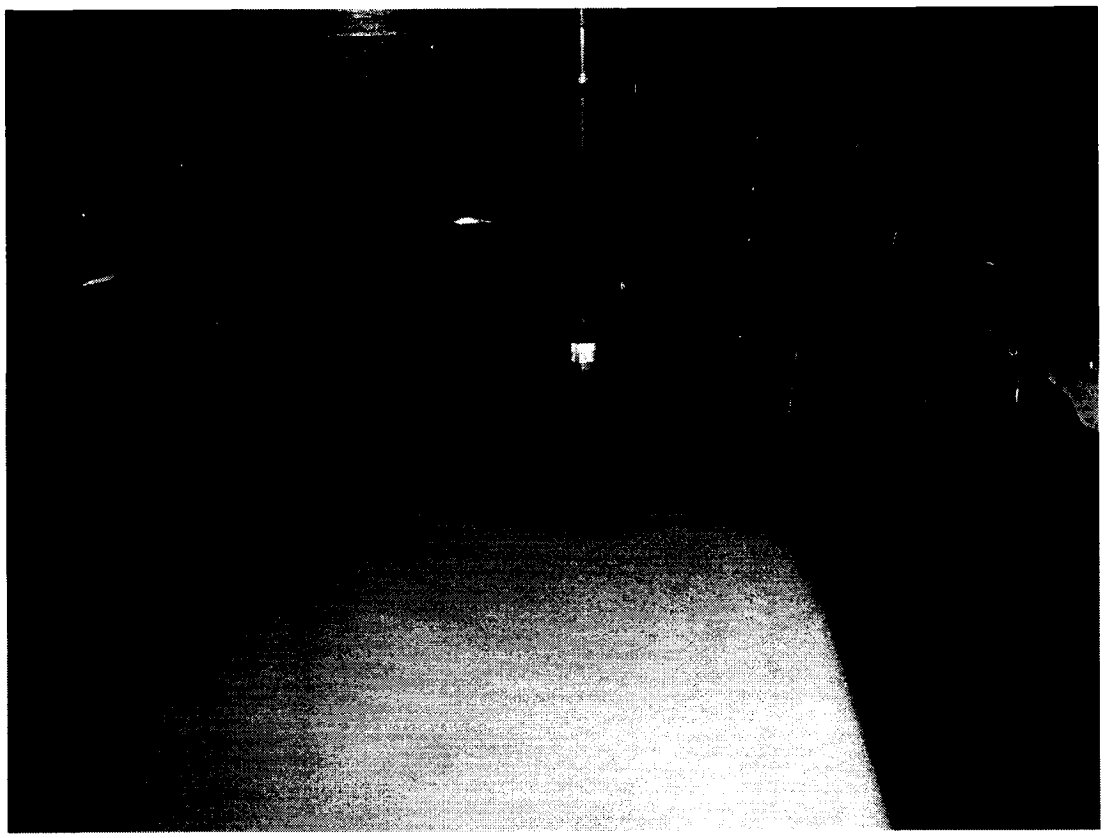

Figure 4.04: Upper slag cover at steady state for new optimized pad.

Figure 4.04 shows the top cover of the slag at steady state, during the experiment with the new optimized pad. Note that under steady state conditions, the area of "slag" around the submerged shroud is not exposed, but the thickness of the slag layer in this region is considerably thinner than that in other parts of the tundish (deep white portion = thick layer of slag, grayish portion = thin layer of slag). A very small portion of surface behind the shroud (at the juncture and apex of the two back walls), is completely exposed. In trying to increase the thickness of the layer of slag near the shroud, after running the flow in steady state condition for some time (e.g. 5 minutes), the condition of the slag layer again reverts to that shown in the figure. i.e. it was reproducible. This

means that there is a strong surface directed flow, which becomes parallel to the surface and is directed from the center of the pad towards the outer regions of the tundish. From the **Figure 4.04**, the symmetry of the flow inside the impact pad area can be seen. As this "slag" condition will probably prevail in actual steelmaking practice with this pad, most of the slag entrainment experiments were done starting from this condition. The first experiments for both the 5 min. and 3 min. draining were done by trying to put more beads near shroud, but for those cases also, the results did not show much difference from the others. The surface condition for those cases shown in **Figure 4.05**.

Figure 4.05: Upper slag layer at steady state with new optimized pad. (pushing more beads near shroud)

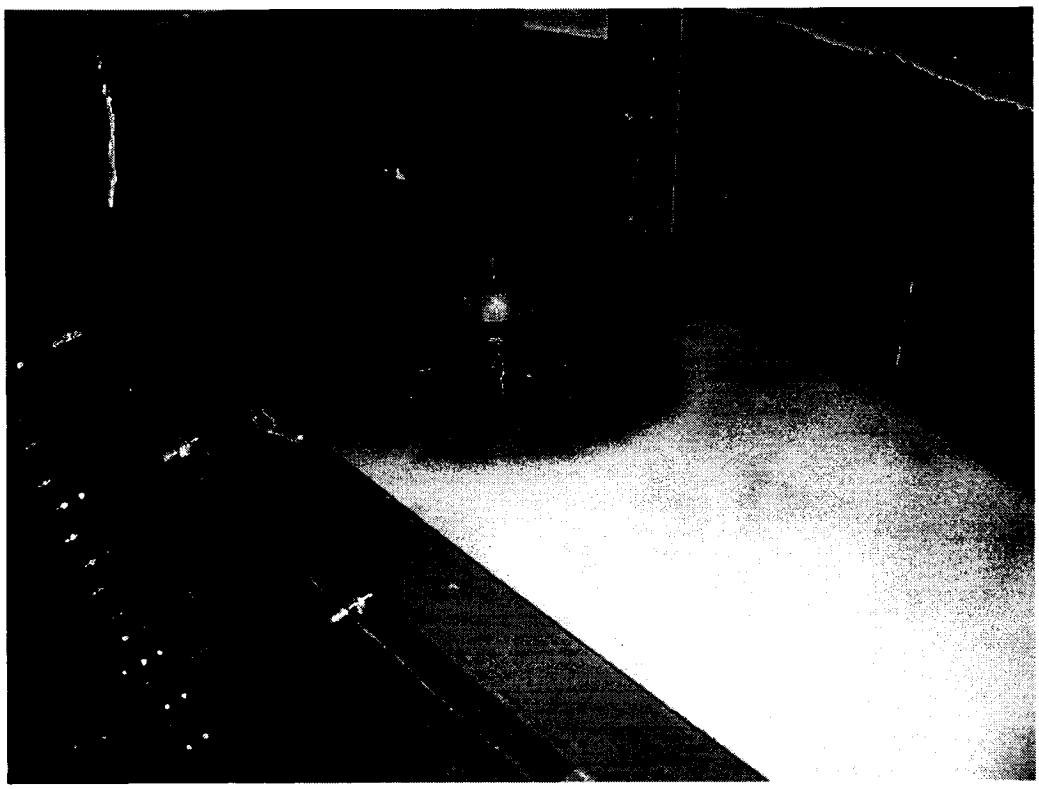

Figure 4.06: Upper slag layer at steady state, using RHI pad.

Figure 4.06 shows the condition of the upper slag layer at steady state, for the RHI pad. From figure 6, it is clear that high tangential flow around and away from the shroud was dominant at steady state. Due to that there was a wide area exposed surrounding the shroud. This "eye" is highly undesirable, leading to steel reoxidation with the formation of alumina inclusions for Al-killed steel grades.

The probable reason may be the size of that pad. It might be larger in proportion to the tundish than optimal.

Some qualitative predictions about the size of the slag droplet are discussed in **Appendix 1**.

4.3 Vortex formation

Table 4.05 & 4.06 below show the critical heights (cm) of liquid in the tundish when stable dimples are formed over the inner and outer nozzles using the RHI pad and the Optimized pad respectively.

Table 4.05: Critical liquid height for dimple formation for RHI pad

Trial#	Height for Inner nozzle (cm)	Height for Outer nozzle (cm)
1	7	6
2	5	3
3	4	3
4	5	8
5	9	12
Average	**6**	**6**
Standard deviation	**2**	**3.8**

Table 4.06: Critical liquid height for dimple formation for Optimized QIT pad

Trial #	Height for Inner nozzle (cm)	Height for Outer nozzle (cm)
1	12.5	11
2	11.5	9.5
3	11	8.5
4	13	10.5
5	12	10
Average	**12**	**10**
Standard deviation	**0.79**	**0.96**

From table 4.05 it can be seen that the standard deviation is high, specifically for the outer nozzle. We all know that residual tangential velocity of the fluid elements promotes onset of vortex. This could be the reason for high variation in results. In other words, if the experiments were started after giving more time to die down the tangential velocities, the results might show lesser standard deviation, which is evident in the results of table 4.06. For those experiments using optimized QIT pad, more time was given for settling down the tangential velocities.

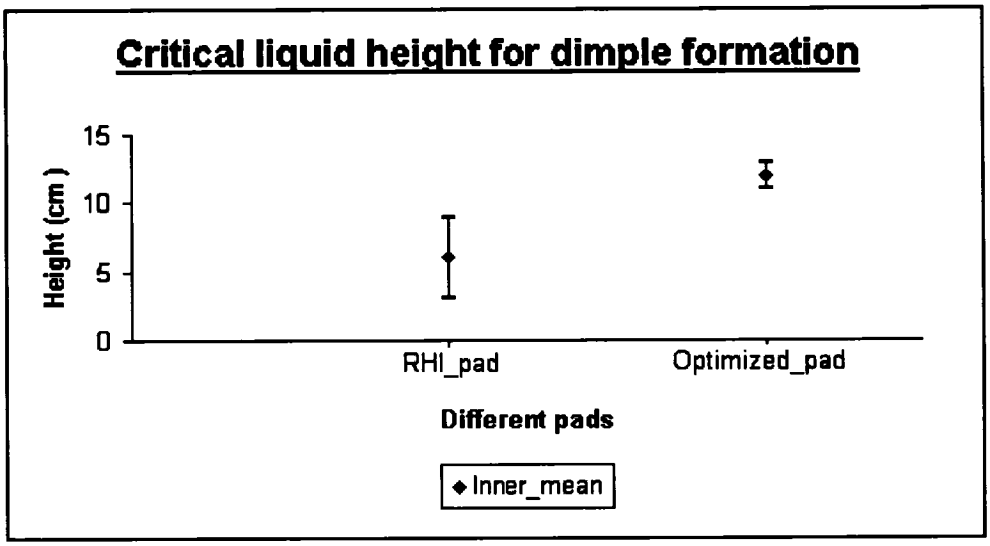

Figure 4.07: Critical liquid height for dimple formation (ie. at the start of vortex formation) over inner nozzles, 2&3.

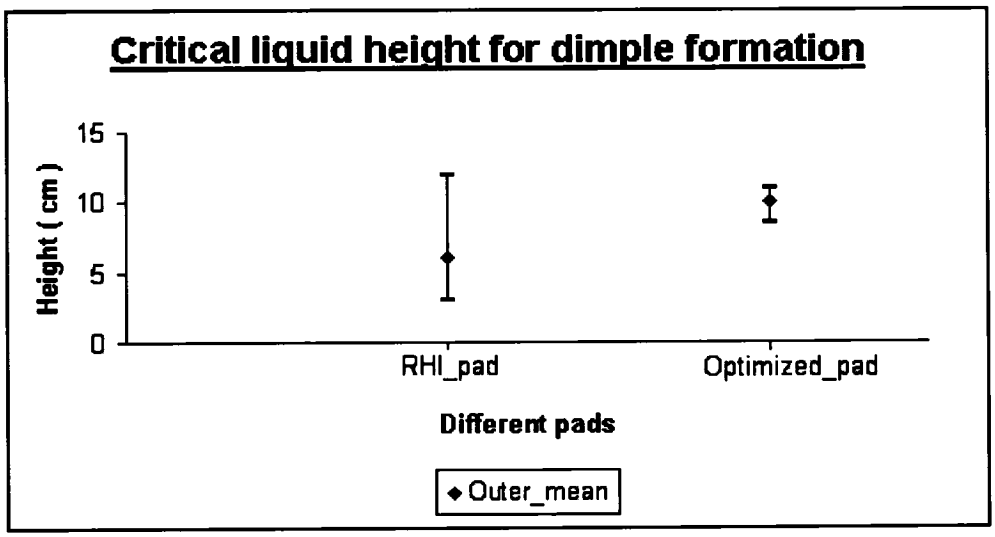

Figure 4.08: Critical liquid height for dimple formation (ie. at the start of vortex formation) over outer nozzles, 1&4

Figure 4.07 & 4.08 shows the height of the liquid in the tundish over the inner and outer nozzles respectively at the time of formation of stable dimple, using two impact pads. It is clear from the figures, that the heights are very low compared to the height of fluid in the tundish at steady state casting operation (50 cm) for all the cases. And as the liquid level does not come down to these levels during 3 or 5 minute draining times, the effect of vortex formation on slag entrainment during a ladle change is insignificant.

4.4 Inclusion Separation Ratio

The inclusion separation ratio is expressed by an index called the Residual Ratio of Inclusions [RRI]. It is expressed on a percentage basis as the following expression:

$$RRI\% = \frac{Number\ of\ Inclusions\ exiting\ the\ outlet}{Number\ of\ Inclusions\ in\ the\ inlet} \times 100$$

As mentioned earlier, the detection of particles was done off line by using the ESZ PAS instrument Inclusion Counter of Heraeus Electro-nite. One thousand milliliter samples of inclusion-laden water were taken for each experimental trials. Three readings for each sample were taken and the average of those three readings were reported.

As the sensitivity of the ESZpas instrument (Inclusion Counter) is poor below 50 micron size and as the number of inclusions over 90 micron size,(i.e. the micro spheres) which are injected at the inlet is very small, the analysis was carried out in four size ranges, namely **50 – 60, 61 – 70, 71 – 80, and 81 – 90** microns.

Table 4.07 shows the results of five trials in the above mentioned size ranges. It shows the average number of particles detected and RRI% calculated from the data for both inner and outer nozzles for five trials. **Figure 4.09** shows the average RRI% at different size ranges of inclusions for the QIT tundish fitted with a RHI pad. The error bars, which show the maximum, mean and the minimum RRI% for each size range, were calculated based on five separate trials.

Similarly, **Table 4.08** shows the results of five trials in the above-mentioned six ranges of inclusions. It lists the average number of particles detected and RRI% calculated from the data for both inner and outer nozzles for five trials.**Figure 4.10** shows the average RRI% vs different size ranges for the Optimized QIT pad. The error bar, which shows the maximum, mean and the minimum RRI% for each size range, were calculated from five separate trials.

Table 4.07: Average number of particles & calculated RRI% Vs different size ranges for RHI pad

		Particle size range (micron)			
Trial		**50 - 60**	**61 - 70**	**71 - 80**	**81 - 90**
1	Inner	133	43	17	9
	Outer	119	34	15	3
	Inlet	603	254	163	113
	RRI%In	**22**	**17**	**10**	**8**
	RRI%Ou	**20**	**13**	**9**	**3**
2	Inner	84	25	10	6
	Outer	129	37	10	5
	Inlet	344	134	66	29
	RRI%In	**24**	**19**	**15**	**21**
	RRI%Ou	**38**	**28**	**15**	**17**
3	Inner	107	34	17	9
	Outer	115	30	12	6
	Inlet	388	167	85	45
	RRI%In	**28**	**20**	**20**	**20**
	RRI%Ou	**30**	**18**	**14**	**13**
4	Inner	113	29	9	3
	Outer	100	33	13	5
	Inlet	349	122	58	32
	RRI%In	**32**	**24**	**16**	**9**
	RRI%Ou	**29**	**27**	**22**	**16**
5	Inner	77	26	7	6
	Outer	101	24	12	5
	Inlet	282	108	49	23
	RRI%In	**27**	**24**	**14**	**26**
	RRI%Ou	**36**	**22**	**24**	**22**

Table 4.08: Average number of particles & calculated RRI% Vs different size ranges for Optimized QIT pad

		Particle size range (micron)			
Trial		**50 - 60**	**61 - 70**	**71 - 80**	**81 - 90**
1	Inner	242	191	111	60
	Outer	145	95	46	22
	Inlet	360	303	183	119
	RRI%In	**67**	**63**	**61**	**50**
	RRI%Ou	**40**	**31**	**25**	**18**
2	Inner	273	202	121	65
	Outer	168	118	53	33
	Inlet	417	340	231	135
	RRI%In	**65**	**59**	**52**	**48**
	RRI%Ou	**40**	**35**	**23**	**24**
3	Inner	295	209	119	69
	Outer	160	116	48	20
	Inlet	405	336	228	131
	RRI%In	**73**	**62**	**52**	**53**
	RRI%Ou	**40**	**35**	**21**	**15**
4	Inner	278	202	106	70
	Outer	172	129	55	33
	Inlet	360	308	178	141
	RRI%In	**77**	**66**	**60**	**63**
	RRI%Ou	**48**	**42**	**31**	**28**
5	Inner	253	193	106	63
	Outer	175	88	52	30
	Inlet	382	327	211	142
	RRI%In	**66**	**59**	**50**	**44**
	RRI%Ou	**46**	**27**	**25**	**21**

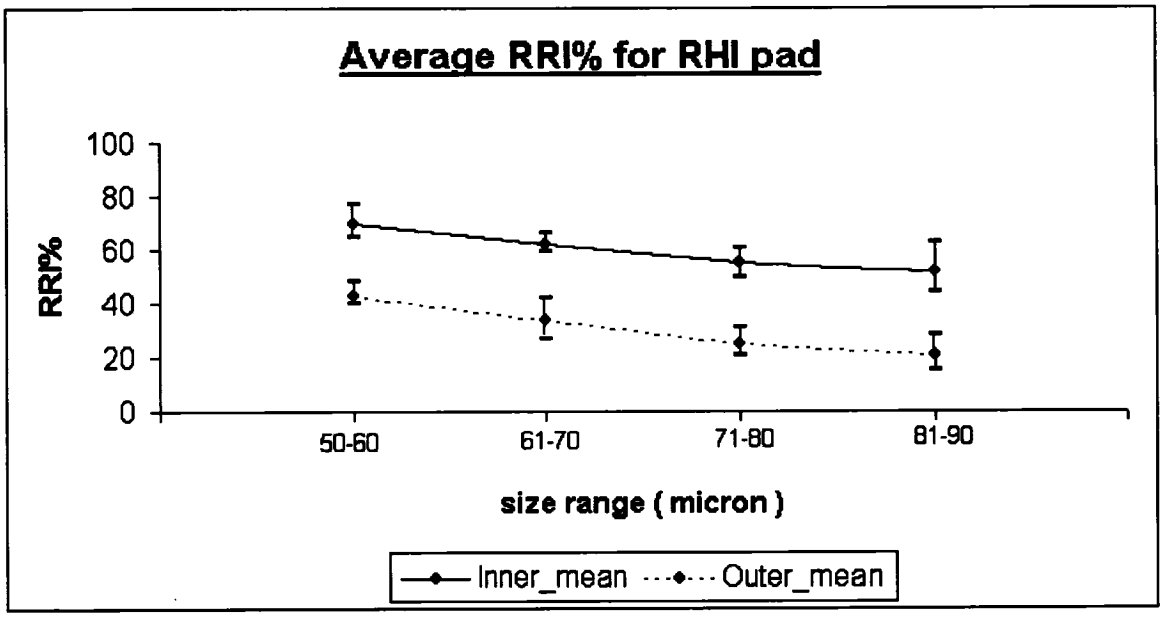

Figure 4.09: Average RRI% of inner and outer nozzles for RHI impact pad.

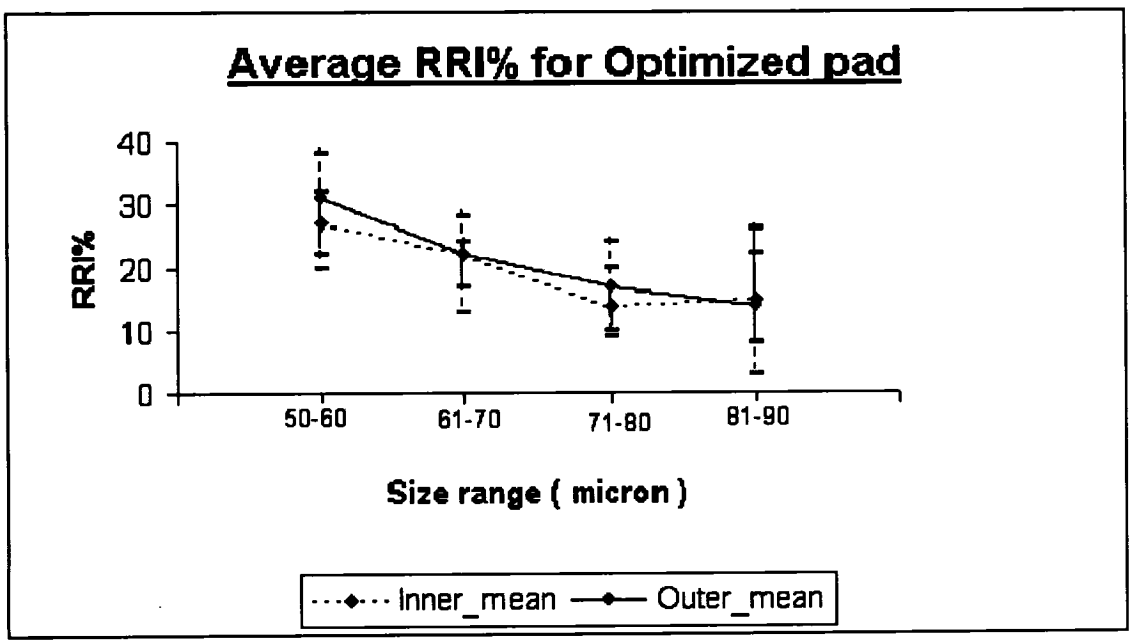

Figure 4.10: Average RRI % of inner and outer nozzles with optimized QIT pad.

For the RHI pad there is a wide gap in the residual ratios for each reported size range between the inner and outer nozzles. This is not present in the result of the QIT optimized pad. This gap indirectly means there is a wide variation in residence times between the inner and outer nozzles.

For the case of the optimized QIT pad, RRI% values for the inner and outer nozzles are very similar. It also indicates that the residence times using this type of pad leads to similar residence time for both inner and outer nozzles, since the rising velocities of these inclusions are relatively small.

Figures 4.11 shows comparative RRI% of inclusions for inner and outer nozzles of the tundish using the two flow modifiers used for study (RHI & QIT optimized pad).

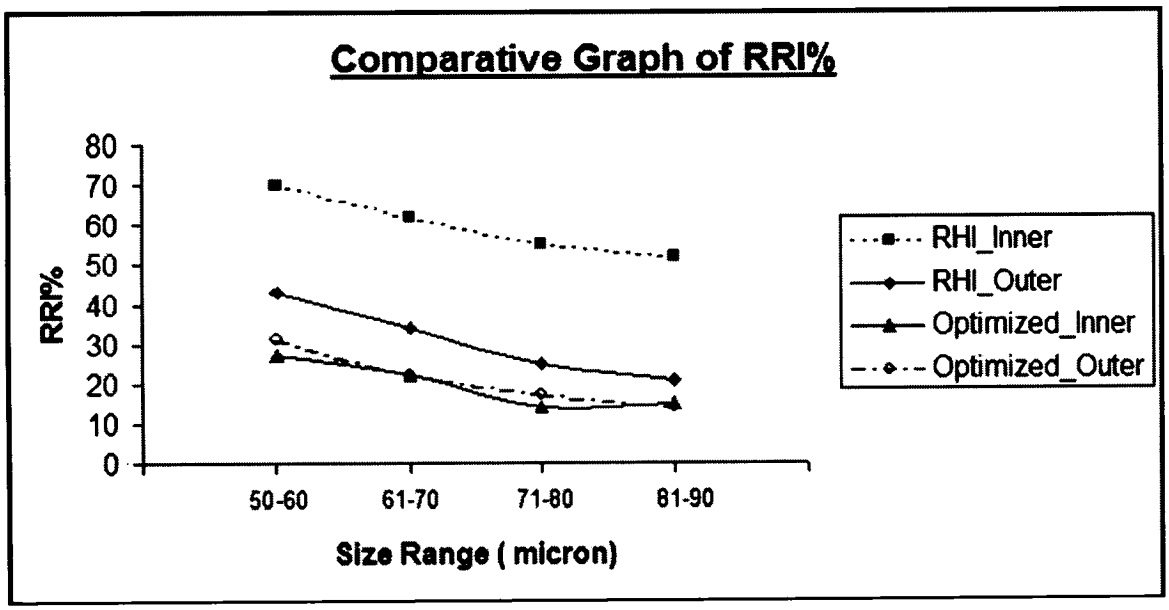

Figure 4.11: Comparative RRI % of inner and outer nozzles using optimized and RHI pad.

It is evident from the results that the optimized QIT pad shows better RRI% values for both the inner and outer nozzles than does the RHI pad. In other words, it can be inferred that it provides a longer mean residence time for inclusion float out than the other pad. It is worth noting that these types of experiments involving the direct measurement of inclusion concentrations have been unique to McGill researchers over the last two decades of this type of tundish research work.

Apart from that, using Table2 (Appendix 2) and extrapolating the curve fitting equation for RRI%, the size and RRI % of the alumina inclusions in steel can be predicted indirectly.

From hydrodynamic principles, the Stokes rising velocity is directly proportional to the square of the radius of spherical particles. This implies that the diameter of particle is expected to have a relation with the upward velocity according to:

$U_t \propto d_p^{\,2}$ [where U_t is the upward velocity and d_p is the diameter of particle]

in the event of stagnant flow conditions over the exit nozzles. In other words one would expect an increase in upward velocity in proportion to the square of the diameter of the particle. Consequently, if we assume the RRI% to be inversely proportional to the upward rising velocity, ie. the greater the upward velocity, the smaller the RRI%. One would expect the RRI% curve to be convex towards the abscissa. Experimentally, this was not observed, the curve being slightly concave. In reality, we can describe the experimental data fairly well in terms of linear equation. The probable reason could be the complex three-dimensional nature of flow inside the tundish and the downward acceleration of fluid immediately above the exit nozzles dominating the Stokesian rising velocity effect of diameter. To conclude, the linear extrapolation of the RRI % curves is likely conservative, given it predicts larger sizes of inclusions than those expected based on Stokesian rising velocities.

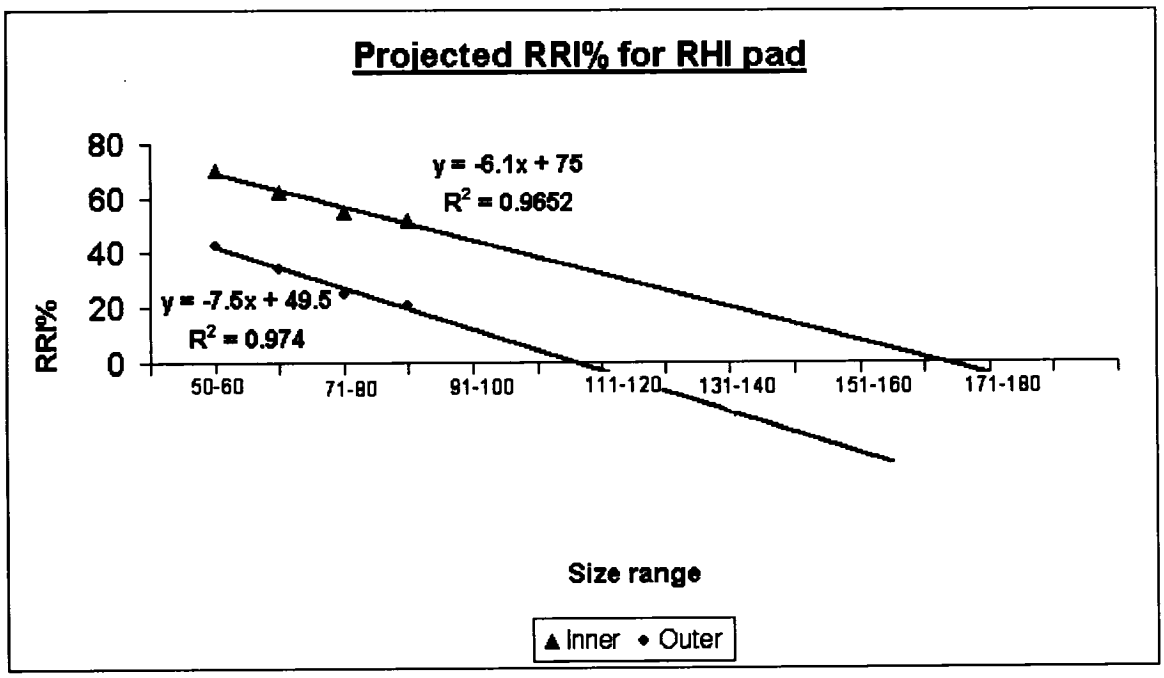

Figure 4.12: Prediction of RRI% for RHI pad.

Figure 4.12 shows the predicted RRI% for micro spheres in water, using the RHI pad. The R^2 values for curve fitting linear equations for both inner and outer are 0.9 which shows how appropriately the results can be describe by the linear equation. The line for the inner nozzles crosses the horizontal axis between the 161-170 micron and the 171-180 micron size ranges for the outer nozzles. This implies that we should not see any inclusion particles beyond those sizes entering the inner nozzles. i.e. particles > 170 micron should be completely floated out in our water model, and should not go to the inner nozzles. For the case of the outer nozzles, the line crosses the horizontal axis after the 101-110 micron size range. So any inclusions >110 micron should not be seen in strands below the outer nozzle. Based on calculations [shown in **Appendix 2**] the corresponding maximum size of alumina particle entering the nozzles would be 127 micron outer nozzles. But the projected size (170 micron) for the inner nozzle does not follow Stokes law as its Reynolds number is greater than 1. So corresponding alumina inclusion size is calculated using intermediate range law [mentioned in **Appendix 1**] and is equal to 199 micron. It means in steel – alumina-inclusion systems, no fully dense inclusions of alumina greater than 199 and 127 microns, should enter the inner and outer nozzles respectively. It implies using this RHI pad; one can expect inclusion even up to the size of 199 micron in inner nozzle, which is not normal in usual practice.

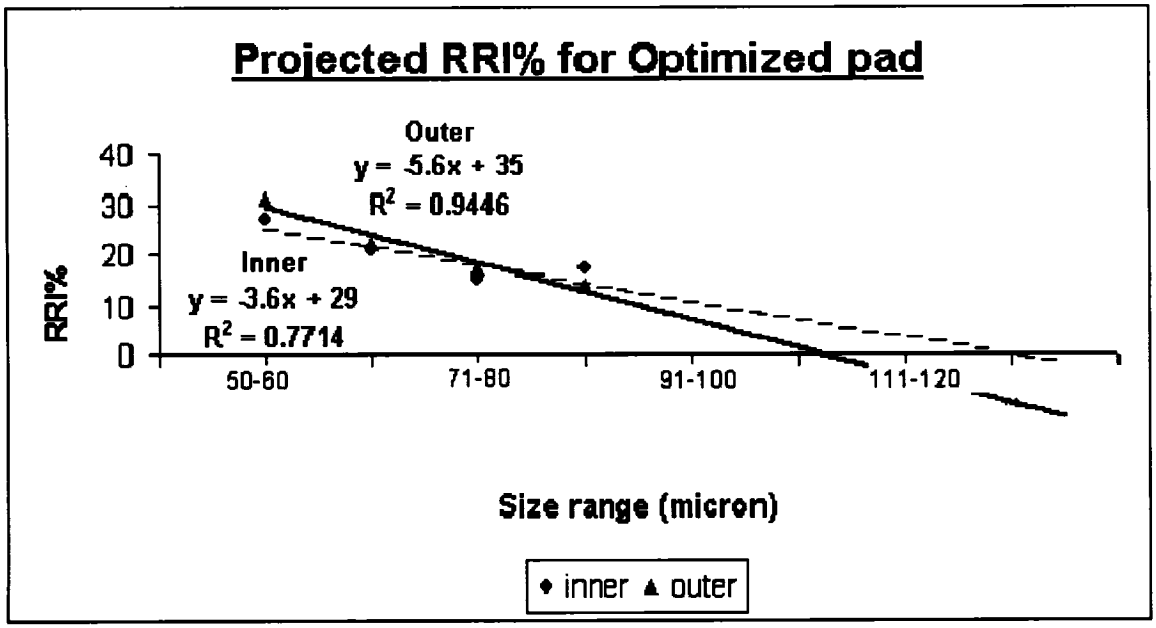

Figure 4.13: Prediction of RRI% for optimized pad.

Figure 4.13 shows the predicted RRI% for micro spheres in water, using the optimized pad. Here also the R^2 values for curve fitting equations for the inner and outer are around 0.8 and 0.9 respectively, and therefore acceptable for engineering purposes.

The line for the inner nozzles crosses the horizontal axis between the 111-120 micron and the 121-130 micron size range. This implies that we should not see any inclusion particles beyond those sizes entering the inner nozzles. i.e. particles > 120 micron should be completely floated out in our water model, and should not go to the inner nozzles. For the case of the outer nozzles, the line crosses the horizontal axis just after the 91-100 micron size range. So the particles >100 micron should not be seen in strands below the outer nozzle. Based on calculations [shown in **Appendix 2**], the corresponding maximum size of alumina particle entering the nozzles would be 133 and 110 micron respectively for inner and outer nozzles. It means in steel – alumina-inclusion systems, no fully dense inclusions of alumina greater than 133 and 110 microns, should enter the inner and outer nozzles respectively.

4.5 Residence time distribution

As mentioned in section 2.2.1, the dead volume, the plug flow volume and the mixed volumes were calculated from the experimental C curves using the following relations:

Mean residence time up-to $\theta = 2$, $\theta_c = \dfrac{\sum_{\theta=0}^{2} C_i \theta_i}{\sum_{\theta=0}^{2} C_i}$

So in dimensional form, the mean residence time = $\theta_c \times \bar{t}$ second.

The dead volume fraction, $\dfrac{V_d}{V} = 1 - \dfrac{Q_a}{Q} \cdot \theta_c = 1 - \left(\sum_{\theta=0}^{2} C_i \Delta\theta \right) \cdot \left(\dfrac{\sum_{\theta=0}^{2} C_i \theta_i}{\sum_{\theta=0}^{2} C_i} \right)$

The dispersed plug volume fraction, $V_{dpv} = (\theta_{min} + \theta_{peak})/2$ where θ_{min} denotes first appearance of tracer and θ_{peak} denotes point peak concentration.

So the mixed volume is given by: $V_{mv} = 1 - V_{dv} - V_{dpv}$.

As the tundish is symmetrical, the area under the overall C curve up to $\theta = 2$, for half of the tundish should be a little bit less than 1 (theoretically area under the full curve, ie. θ = infinity, should be 1). This area is calculated according to the following the relation:

Area under the curve up-to $\theta = 2$, $\dfrac{Q_a}{Q} = \sum_{\theta=0}^{2} C_i \Delta\theta$.

The tundish under consideration has an operational volume of $1.76 m^3$ and while the flow rate of water through it is 172 L/min.

So the nominal residence time is = $\dfrac{1.76 \times 1000}{172} \times 60 = 613.9 \sim 614$ s

Table 4.09 shows the average residence time for the tundish, average residence time for the inner and outer nozzle, overall dead volume percent, overall plug flow volume percent, overall mixed flow volume percent and the area under the curve up-to $\theta = 2$, calculated from experimental data for the tundish using the Optimized QIT pad.

Table 4.10 shows the above variables for the tundish fitted with a RHI pad.

Table 4.09: Different variable calculated from C curve using Optimized QIT pad

Trial #	Average Residence time, s	Residence time inner s	Residence time outer s	Dead volume%	Plug flow volume%	Mixed volume %	Area under C curve up to theta=2
1	229.45	231.39	227.19	60.76	7.41	31.83	1.05
2	235.49	242.85	227.44	62.41	8.51	29.08	0.98
3	235.08	231.42	239.49	63.24	8.55	28.21	0.96
4	245.62	241.29	250.29	63.19	8.87	27.94	0.92
5	230.02	221.74	240.71	62.91	7.78	29.31	0.99
Avg.	**235.132**	**233.738**	**237.024**	**62.502**	**8.224**	**29.274**	**0.98**

Table 4.10: Different variable calculated from C curve using RHI pad

Trial	Residence time, s	Residence time inner s	Residence time outer s	Dead volume%	Plug flow volume%	Mixed volume %	Area under C curve up to theta=2
1	208.9	176.4	230.3	69.7	8.18	22.12	0.89
2	213.1	178.7	231.8	66.54	8.26	25.2	0.87
3	197.4	161.6	220.8	71.52	8.06	20.42	0.89
4	212.1	177.7	233.4	68.72	7.98	23.3	0.91
5	213.7	177.7	237.5	68.98	8.06	22.96	0.89
Avg.	**209.04**	**174.42**	**230.76**	**69.092**	**8.108**	**22.8**	**0.89**

From Table 4.09 the values of calculated residence time for inner and outer nozzles are fairly close for the Optimized QIT pad. Table 4.10 shows a wide difference in equivalent values using the RHI pad.

The result is consistent with the results obtained from the RRI% and Slag Entrainment Trials done using these pads.

Using the RHI pad it can be seen from the Figure 4.09, that the RRI% for the outer nozzle is much less than that for the inner nozzle. The probable cause might be the

difference in residence time. Which is confirmed by the results shown in Table 4.10. The individual residence time for the outer nozzle is much higher than that for the inner and which provided more time for inclusions to float out, effecting lower RRI% in all reported size ranges. From Figure 4.02 and 4.03, it can be noticed that there is almost no beads found in outer nozzles, while a significant number of beads were found for the inner nozzles. The lower residence time for the inner nozzle and wide difference in the residence time between the inner and outer nozzle could be the reason for this result.

The same arguments can be used to explain the results for the Optimized QIT pad. As the residence time for both the nozzles are more or less similar, the RRI% and also the number of beads in slag entrainment trials were similar for both the nozzles.

Apart from that, the RTD results confirm the trend of RRI% results shown in Figure 4.11. From the Figure 4.11, the RRI% is highest for the case of inner nozzle using RHI pad. Results from the Table 4.10 also confirm the validity of this data showing least residence time for that case (inner nozzle with RHI pad). The other trends are also consistent, as can be seen from the other data from table 4.10 and 4.11.

Another important point is worth mentioning is that, the dead volume percentage for the RHI pad is higher than that for Optimized QIT pad. In both cases, the values are very high. This indicates that a substantial portion of the tundish remains unutilized. It also indicates that, during designing a pad, the dead volume percentage should also be considered.

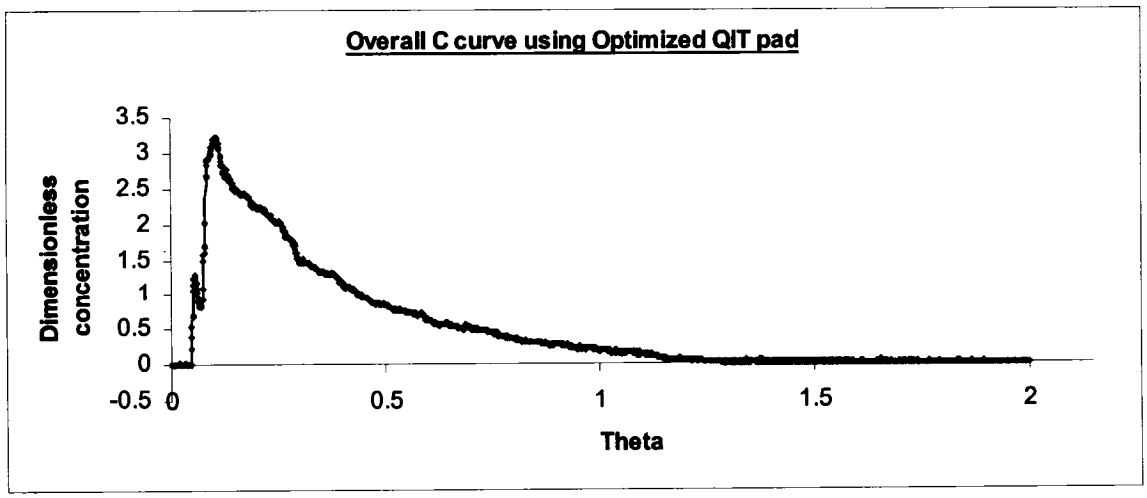

Figure 4.14: Representative overall C curve using Optimized QIT pad.

Figure 4.14 shows the overall C curve generated from the experimental data using the Optimized QIT pad. There are two peaks in the curve. The first peak is due to short-circuiting of the flow and occurs mainly in the inner nozzle as can be seen from Figure 4.15.

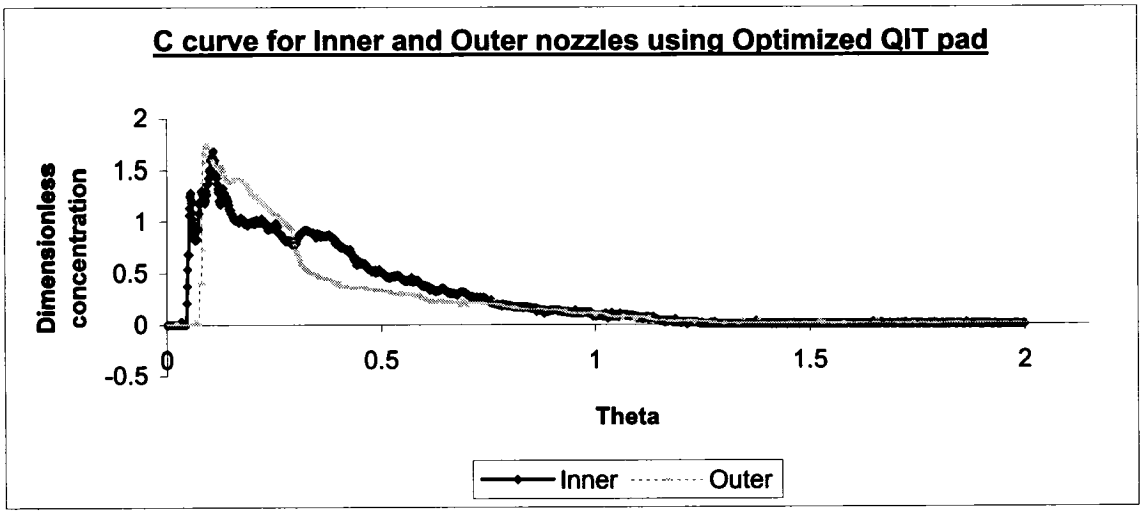

Figure 4.15 : Representative C curve for Inner and outer nozzles using Optimized QIT pad

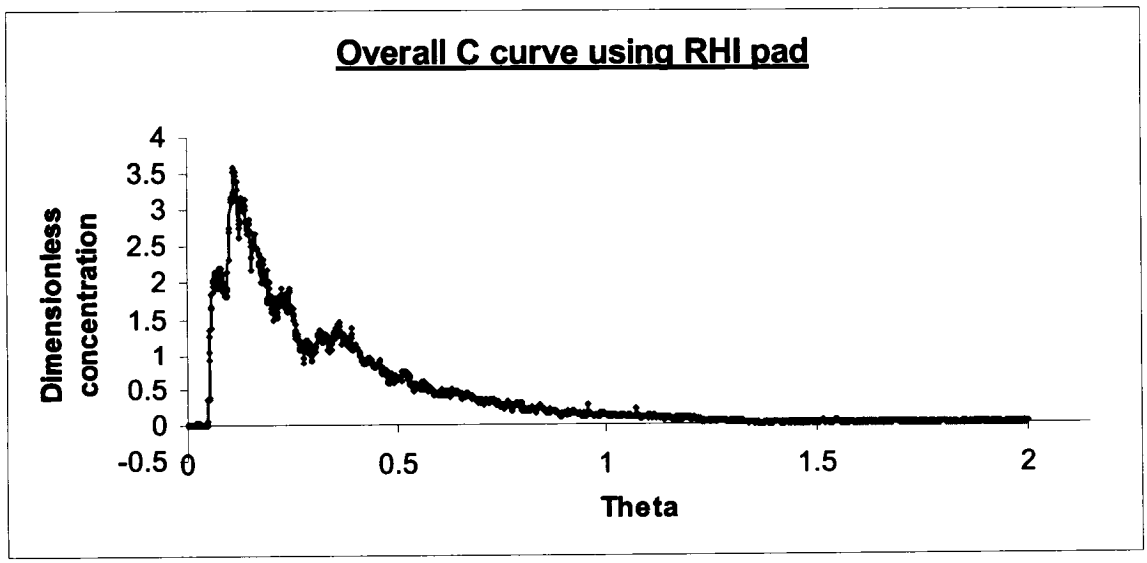

Figure 4.16: Representative overall C curve using RHI pad.

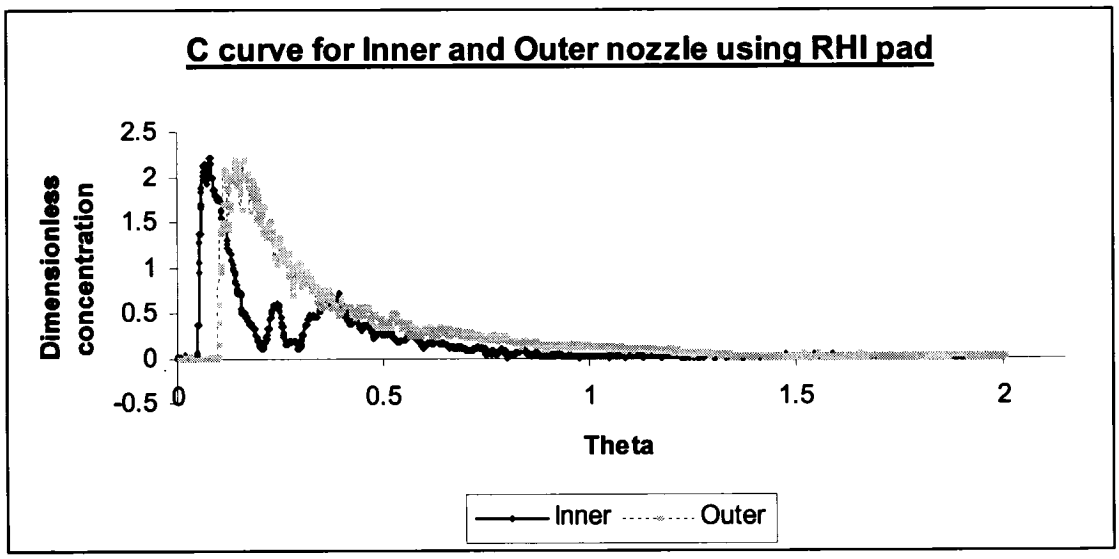

Figure 4.17: Representative C curve for Inner and outer nozzles using RHI pad .

Figure 4.16 shows the overall C curve of the tundish using RHI pad. Here also two peaks are clear in the curve. The C curves for inner and outer nozzles are shown in figure 4.17.

5. SUMMARY AND CONCLUSIONS

From the results obtained from the experiments carried out during physical simulations of RTIT 's(QIT) 4-strand delta shaped tundish, using the 'RHI pad, and the 'Optimized pad' as flow modification furniture, the following conclusions can be drawn:

1) The RHI pad prevented any slag beads reporting to the outer nozzles but a high number exited through the inner nozzles during both 5 min and 3 min draining experiments. The Optimized pad showed a more even distribution in terms of number of beads for both inner and outer nozzles for both types of experiments. From these results it can be concluded that both inner and outer strand during casting, using Optimized pad, is expected to give a more uniform quality of product during transient operations.
2) The height of the water for dimple formation were very low for both types of impact pads. This indicates for both cases there would be no vortex formation, which would have lead to severe slag entrainment.
3) From the point of view of inclusion separation, the results suggest that with the RHI pad one can expect bigger inclusions, with a higher percentage of occurance vs steel poured using an Optimized pad.
4) From the RTD analysis using the Optimized QIT pad, the overall residence time calculated is more than that for the RHI pad. The dead volume is less for the optimized QIT pad. Whereas the plug flow volume and mixed volume percentage are more for the case with Optimized QIT pad. The residence time for the inner and outer nozzles are more even for the optimized QIT pad. All of these results are in accordance with the results of RRI and slag entrainment experiments.

Collectively all the experimental results show, between the RHI pad and the Optimized QIT pad, that the latter would perform better in terms of steel quality, and uniformity of steel product inclusion levels.

APPENDIX 1

Calculation of size of slag droplet, corresponding to the size of the beads used in the water model:

The terminal velocity of a particle in a fluid follows different laws for different flow regimes defined by their associated Reynolds numbers. The equivalent slag particle diameter or velocity, is calculated using the laws of motion specific to that flow regime and then cross checking the Reynolds number using the calculated rising velocity value, so as to verify whether it falls actually in that regime, or not. It is customary to investigate the Stoke's regime for viscous flows, first.

The basic assumption for all these calculations is that the particles are rising through a stationary liquid.

Table A.01: Physical properties of the materials used for modelling slag entrainment and those of liquid steel and slag.

Material	Kinematic viscosity $\upsilon = (\mu / \rho)$ (m^2/s)	Density (kg/m^3)
Liquid Steel (1600 °C)	0.913×10^{-6}	~ 7000
Liquid Slag	-	~ 3200 - 3600
Water (20 °C)	10^{-6}	1000
High density Polyethylene	-	~ 935

Table A.01 shows physical properties of the materials.

Table A.02: Size of randomly sampled high density polyethylene beads and their mean diameter

Sl. Number	Reading 1(r_1), mm	Reading 2 (r_2) mm	Reading 3 (r_3) mm	$r_1 * r_2 * r_3$ mm^3	Geometric Mean, mm
1	3.5	5	3.6	63	3.98
2	3.3	2.6	3.0	25.74	2.95
3	3.3	3.8	3.6	45.14	3.56
4	2.2	3.1	2.5	17.05	2.57
5	2.8	3.5	4.1	40.18	3.43
6	2.8	2.9	1.9	15.43	2.49
7	3.0	3.4	2.4	24.48	2.9
8	4.6	3.5	3.0	48.3	3.64
9	3.4	3.5	2.6	30.94	3.14
Average :					3.2

Table A.02, shows the size of 9 randomly sampled beads and their mean diameter.

Stokes law regime:

Stokes law is valid for Reynolds number less than or equal to 0.1 for spheres in stagnant medium. For most engineering purposes the allowable Reynolds number in this region is 1, rather than 0.1.

Here the Reynolds number is defined as:

$$\mathrm{Re} = \frac{U d_p}{\upsilon_l} \quad \text{.....(A1)}$$

The Stokes rising velocity can be written as:

$$U = \frac{(1 - \rho_p / \rho_l) g d_p^{\,2}}{18 \upsilon_l} \quad \text{..... (A2)}$$

Using the properties given in **Table A.01,** and the bead sizes given in **Table A.02,** the Stokes velocities of the beads (calculated using equation A2) and their corresponding Reynolds numbers (calculated using equation A1) are given in **Table A.03.**

Table A.03: Mean bead size, Stokes velocity and corresponding Reynolds numbers

Bead size (mm)	Stokes velocity (m/s)	Reynolds number
3.98	0.56	2233
2.95	0.31	909
3.56	0.45	1598
2.57	0.23	601
3.43	0.42	1430
2.49	0.22	547
2.9	0.30	864
3.64	0.47	1709
3.14	0.35	1097
Average = 3.2	0.36	1161

It is clear from the **Table A.03** that the Reynolds numbers are not in the Stokes range. So the assumption that the polyethylene particles follow Stokes law is not valid and predicting rising velocities that are almost 10X too high. So we have to investigate the intermediate range for submerged spheres in a Newtonian liquid.

Intermediate law regime:

This flow regime is valid for Reynolds numbers between 2 and 500. In this range, the friction factor *(f),* is related to the Reynolds number Re, according to the following relation.

$$f = \frac{18.5}{\mathrm{Re}^{\frac{3}{5}}} \quad \text{.....(A3)}$$

Now from the first principles, the buoyancy force of the particle is balanced against the drag force in steady in steady translation:

$$\frac{4}{3}\pi\left(\frac{d_p}{2}\right)^3(\rho_l - \rho_p)g = fAk \quad \text{.....(A4)}$$

where A = projected area of the spherical slag particle = $\pi\left(\frac{d_p}{2}\right)^2$

k = kinetic energy of the liquid per unit volume= $\frac{1}{2}\rho_l U^2$.

Using equation (A3) & (A4) we can calculate the upward velocity of beads.

Table A.04, below, shows the upward velocity of the particles and corresponding Reynolds numbers for the bead sizes. The Reynolds numbers are in the intermediate range.

Table A.04: Mean bead size, rise velocity and corresponding Reynolds numbers

Bead size (mm)	Upward velocity (m/s)	Reynolds number
3.98	0.075	297
2.95	0.053	156
3.56	0.062	234
2.57	0.045	116
3.43	0.063	216
2.49	0.044	109
2.9	0.052	151
3.64	0.067	245
3.14	0.057	179
Average = 3.2	0.058	186

Now knowing the upward velocity and using equation (A3) & (A4), we can calculate the corresponding diameter of slag droplet in steel.

Table A.05: Rise velocities, Diameter of the slag droplets, and Reynolds numbers

Upward velocity (m/s)(slag)	Slag droplet Diameter(mm)	Reynolds number
0.075	1.025	84
0.053	0.757	44
0.066	0.917	66
0.045	0.656	32
0.063	0.880	61
0.044	0.643	31
0.052	0.744	42
0.067	0.929	68
0.057	0.806	50
0.058 (for average diameter)	0.819	52

Table A.05 shows the diameter of the slag droplets, corresponding to the upward velocities and Reynolds numbers in Table 4. The Reynolds numbers are again in the intermediate range, so the assumption of flow behaviour in the intermediate range is valid.

So looking at column 2 of table A.05, we can qualitatively say that the slag droplet diameter, that can be detected in steel could be of the size indicated in the column and is ~four (3.9) times smaller than the beads used in the water modeling experiments. Apart from that, the number of beads in the strands can represent the number of slag droplets that could be entrapped, if the slag layer over steel is broken into the droplet sizes indicated in the second column in table A.05, when the steel jet first plunges into the tundish following a ladle change.

APPENDIX 2

Calculation of the size of alumina inclusions corresponding to the size of the hollow glass micro-spheres.

According to earlier researchers, it is reasonable to assume that inclusions generated in molten steel as products of steel deoxidation, follow Stokes law. So using Stokes law we can determine the diameter of alumina inclusions that would correspond to the diameter of the hollow glass micro-spheres.

Stoke's law is valid for Reynolds number less than or equal to 0.1, but for most engineering purposes the allowable Reynolds number in this region is 1.

Here the Reynolds numberis :

$$\mathrm{Re} = \frac{U d_p}{\upsilon_l} \quad \text{.....(A5)}$$

The Stokes rising velocity can be written as:

$$U = \frac{(1 - \rho_p / \rho_l) g d_p^{\,2}}{18 \upsilon_l} \quad \text{..... (A6)}$$

We can calculate the representative size of alumina inclusions in steel using the values of properties mentioned in **Table A.06** and the above-mentioned relations,

Table A.06: Physical properties of the materials used for modelling inclusion separation and those of liquid steel and dense alumina.

Material	Size Range (micron)	Density (kg/m^3)	Viscosity (m^2/s)
Water	-	1000	10^{-6}
Hollow glass micro spheres (sodium borosilicate) (ECCOSPHERE IG 101)	5 – 150	350	-
Liquid Steel	-	~7000	0.913×10^{-6}
Fully dense alumina inclusion		~3900	-

Table A.07 shows the size of the alumina particles that corresponds to the size of the particle used for physical simulation of inclusion separation.

Table A.07: Size of micro spheres & corresponding size of alumina inclusion considering behavior in Stoke's region.

Size of micro-sphere	Size of alumina inclusion
50	58
65	64
70	75
75	81
80	87
85	93
90	98
95	104
100	110
105	116
110	122
115	127
120	133
125	139
130	145
135	150

It was already reported [12] that the fraction of the particles greater than 150 microns are generally small under standard operating conditions (i.e. outside of major excursions caused by operating practices such as ladle changes, or slag vortexing, etc.). As such equivalence calculations are only shown up to 150 microns.

REFERENCES

1. Levenspiel O.; Chemical Reaction Engineering, John Wiley & Sons , 2nd Edition, 1972.
2. Guthrie R. I. L; Engineering in Process Metallurgy, Oxford University Press, 1993.
3. Szekeley J, Ilegbussi O; The Physical and Mathematical Modeling of Tundish Operations, Springer-Verlag, 1989.
4. Mazumdar, D., Guthrie, R. I. L.; The Physical and Mathematical Modeling of Continuous Casting Tundish Systems, ISIJ International, 39(6), 1999, pp 524-547.
5. White F. M.; Fluid Mechanics, McGraw-Hill, 3rd edition, 1994.
6. Bird R. B., Stewart W. E. and Lightfoot E. N.; Transport Phenomena, John Wiley and Sons, 1960.
7. Gaskell D.R.; An Introduction to Transport Phenomena in Engineering, Macmillan Publishing Company, 1992.
8. Sankarnarayanan R.; Modelling of Slag Entraining Funnel Formation ('Vortex') During Liquid Metal Transfer Operations, PhD Thesis, McGill University, 1994.
9. Kim H. B.; Modelling of Transport Phenomena in a Delta-shaped Four Strand Tundish, PhD thesis, McGill University, 2003.
10. de Kock D. J.; Optimal tundish Design Methodology in a Continuous Casting Process, PhD thesis, University of Pretoria, 2005.
11. Tanaka S.; Modelling Inclusion Behaviour and Slag Entrainment in Liquid Steel Processing Vessels, PhD thesis, McGill University, 1986.
12. Nakajima H.; On the Detection and Behaviour of Second Phase Particles in Steel Melts, PhD thesis, McGill University, 1986.
13. Cramb A.W. and Byrne M.; Tundish Slag Entrainment at the Bethlehem's Burn Harbor (Indiana) Slab Caster, Steelmaking Conference Proceedings, ISS-AIME, 67, 1984, pp 5-13.
14. Steffen R.; Fluid Flow Phenomena of Metal and Slag During Drainage of Metallurgical Vessels, Proceedings of International Conference Secondary Metallurgy, Aachen, West Germany, September, 1987, Preprints, pp 97-118.

15. Vargas-Zamora A., Morales R. D., Diaz-Cruz M., Palafox-Ramos J., Barreto-Sandoval J. and De J.; Inertial and Buoyancy Driven Water Flows Under Gas Bubbling and Thermal Stratification Conditions in a Tundish Model, Metallurgical and Materials Transactions B, Process Metallurgy and Materials Processing Science, 35B(2), 2004, pp 247-257.
16. Aguilar-Corona A., Morales R. D., Diaz-Cruz M., Palafox-Ramos J.and Demedices L. G.; Thermal Stratification of Steel Flow in Tundishes With Off-centered Ladle Shrouds Using Different Flow Control Designs, Canadian Metallurgical Quarterly, 42(4), 2003, pp 455-464.
17. Kim H. B., Guthrie R. I. L., Isac M.and Thibau R.; The Effect of Flow Modifiers on the Hydrodynamic Performance of a Delta-shaped, Four-strand Tundish, ISSTech Conference Proceedings, 1st, Indianapolis, IN, United States, Apr. 27-30, 2003, pp 1394-1403.
18. Martinez R. and Solis T. H.; Modelling of Asymmetrical Tundishes, Steelmaking Conference Proceedings, 1992, pp 893-898.
19. Knoepke J. and Mastervich J.; Water Modeling Inland Steel's No. 3 Combination Caster Tundish, Inland Steel Company, East Chicago, Indiana, Proc. of the Steelmaking Conference, TMS, 1986, pp 777-788.
20. Mazumdar D., Yamagulu G., Shankarnarayanan R. and Guthrie R. I. L.; Similarity Considerations in the Physical Modeling of Steel Making Tundish Systems, Steel Research, 66(1), 1995, pp 14-19.
21. Szekely J., Evans J.E. and Brimacombe J. K.; The Mathematical and Physical Modeling of Primary Metals Processing Operations, John Wiley & sons, 1988.
22. Sahai Y. and Burval M. D.; Validity of Reynods and Froude Similarity Criteria for Water Modeling of Melt Flow in Tundishes, Electric Furnace Conference Proceedings, 1992, pp 469-474.
23. Godiwalla K. M., Sinha S. K., and Sivaramakrishnan; Water Model Simulation of Tundish Flow Under Varying Conditions, Steel Research, 65(7), 1994, pp 14-19.
24. Sahai Y. and Emi T.; Melt Flow Characterization in Continuous Casting Tundishes, ISIJ International, 36 (6), 1996, pp 667-672.

25. Damle C. and Sahai Y.; A Criterion for Water Modeling of Non-isothermal Melt Flows in Continuous Casting Tundishes, ISIJ International, 36 (6), 1996, pp 681-689.
26. Mazumdar D., Yamanogulu G.and Guthrie R. I. L.; Hydrodynamic Performance of Steelmaking Tundish Systems: A Comparative Study of Three Different Tundish Designs, Steel Research, 68 (7), 1997, pp 293-300.
27. Shirabe K. and Szekely J.; A Mathematical Model of Fluid Flow and Inclusion Coalescence in the R-H Vacuum Degassing System, Trans. ISIJ, 23, 1983, pp 465-.
28. Singh S. and Koria S. C.; Physical Modeling of Steel Flow in Continuous Casting Tundish, Ironmaking and Steelmaking , 20(3), 1993, pp 221-230.
29. Singh S.and Koria S.C., Physical Modeling of the Effects of the Flow Modifier on the Dynamics of Molten Steel Flowing in a Tundish, ISIJ International, 34 (10), 1994, pp 784-793.
30. Singh S. and Koria S. C.; Study of Fluid Flow in Tundishes Due to Different Types of Inlet Streams, Steel Research, 66(7), 1995, pp 294-300.
31. Singh S. and Koria S. C.; Model Study of the Dynamics of Flow of Steel Melt in the Tundish, ISIJ International, 33 (12), 1993, pp 1228-1237.
32. Joo S. and Guthrie R. I. L.; Inclusion Behavior and Heat-transfer Phenomena in Steelmaking Tundish Operations: Part I. Aqueous Modeling, Metallurgical and Materials Transactions B, 24B, 1993, pp 755-765.
33. Joo S., Han J. W. and Guthrie R. I. L.; Inclusion Behavior and Heat-transfer Phenomena in Steelmaking Tundish Operations: Part II. Mathematical Model for Liquid Steel in Tundish, Metallurgical and Materials Transactions B, 24B, 1993, pp 767-778.
34. Joo S., Han J. W. and Guthrie R. I. L.; Inclusion Behavior and Heat-transfer Phenomena in Steelmaking Tundish Operations: Part III. Applications – Computational Approach to Tundish design, Metallurgical and Materials Transactions B, 24B, 1993, pp 779-788.
35. Wen G., Zhang L., Tang P., Su Z., Zhu M., Gu W., Zhao K.and Song G.; Physical and Mathematical Simulation of Fluid Flow, Heat Transfer and Particle Motion in

a 6-strand Continuous Casting Tundish, ISSTech Conference Proceedings, 1st, Indianapolis, IN, United States, Apr. 27-30, 2003, pp 1729-1740.

36. Sahai Y. and Ahuja; Fluid Flow and Mixing of Melt in Steelmaking Tundishes, Ironmaking and Steelmaking, 13 (5), 1986, pp 241-247.
37. Chiang L. K.; Water Modeling of IPSCO's Slab Caster, Steelmaking Conference Proceedings, 1992, pp 437-450.
38. Kou Sindo; Transport Phenomena and Materials Processing, John Wiley & Sons, 1996.
39. Couller M. M., Love D.B. and Patil B.V.; Use of Flow Modifiers to Improve Performance of a Tundish, Steelmaking Conference Proceedings,1997, pp 313-324.
40. Sankarnarayanan R. and Guthrie R. I. L.; Slag Entraining Vortexing Funnel Formation During Ladle Teeming: Similarity Criteria and Scale up Relationships, Ironmaking and Steelmaking, 29(2), 2002, pp 147-153.
41. Quick M.G.; Scale Relationships Between Geometrically Similar Free Spiral Vortices, Civil engineering and public works review, 57,674,OCT, 1962, pp 1135-1138.
42. Anwar H. O.; Flow in Free Vortex, Water power, April, 1965, pp 153-161.
43. Kamel M. Y. M.; The Effect of Swirl on the Flow of Liquids Through Bottom Outlets, Fluids Engineering Conference, New York, ASME paper 64WA/FE-37, 1964, pp 1-9.
44. Daggett L. L. and Keulegan G. H.; Similitude in Free Vortex Formations, Proceedings of The ASCE, Journal of The Hydraulics Division, 100, HY11, November, 1974, pp 1565-1568.
45. Wolf M. M.; History of Continuous Casting, Steelmaking Conference Proceedings, Iron & Steel Society, Warrendale, PA,1992, pp. 83-137.
46. Heraeus Electro-Nite, ESZ-PAS inclusion counter operation manual, version 2.1m, June, 2004.